Self-Organized Inorganic-Organic Phyllosilicate Hybrids:

Investigating Bridging Ligands and Imprinting Methods for Heavy Metal Ion Adsorption

by

Thomas Bizley

A thesis submitted in partial fulfillment

of the requirements for the degree of

Master of Science (MSc) in Chemical Sciences

The Faculty of Graduate Studies

Laurentian University

Sudbury, Ontario, Canada

THESIS DEFENCE COMMITTEE/COMITÉ DE SOUTENANCE DE THÈSE

Laurentian Université/Université Laurentienne

Faculty of Graduate Studies/Faculté des études supérieures

Title of Thesis Titre de la thèse	Self-Organized Inorganic-Organic Phyllosilicate Hybrids: Investigating Bridging Ligands and Imprinting Methods for Heavy Metal Ion Adsorption
Name of Candidate Nom du candidat	Bizley, Thomas
Degree Diplôme	Master of Science
Department/Program Département/Programme	Chemical Sciences
Date of Defence Date de la soutenance	October 7, 2014

APPROVED/APPROUVÉ

Thesis Examiners/Examinateurs de thèse:

Dr. Louis Mercier
(Supervisor/Directeur(trice) de thèse)

Dr. Joy Gray-Munro
(Committee member/Membre du comité)

Dr. Jeff Shepherd
(Committee member/Membre du comité)

Dr. Rémi Beaulac Acting Dean, Faculty of Graduate Studies
(External Examiner/Examinateur externe)

Approved for the Faculty of Graduate Studies
Approuvé pour la Faculté des études supérieures
Dr. David Lesbarrères
M. David Lesbarrères
Acting Dean, Faculty of Graduate Studies
Doyen intérimaire, Faculté des études supérieures

ACCESSIBILITY CLAUSE AND PERMISSION TO USE

Abstract

The talc-like organoclay, MgSi-b-*en*, was synthesized using a bridged organosilane precursor containing the ethylenediamine moiety through the sol-gel process. Characterization of the material revealed disordered, interconnected phyllosilicate sheets, with a high surface area and a composition resembling natural talc. Ethylenediamine moieties were successfully incorporated into the structure of MgSi-b-*en*. The material performed well as an adsorbent of the heavy metal ions Cu(II), Ni(II), and Pb(II). The adsorption capacities of the adsorbent were very high. Multi-component adsorption tests revealed a specific adsorption preference of Pb > Cu > Ni. An ion-imprinting technique was performed to alter the specificity of the adsorbent. The procedure produced organoclays with cavities matching the size of the metal ion used in the synthesis. In the presence of larger ions, the two imprinted adsorbents, MgSi-b-*en*(-Cu) and MgSi-b-*en*(-Ni), displayed higher adsorption capacities and selectivity coefficients towards Cu(II) and Ni(II) ions, respectively.

Keywords

Silicon, Clay, Metal Adsorption, Remediation, Functionalize, Imprint, Porous, Selectivity, Specificity

Acknowledgements

I would first like to thank my family and friends who have supported and loved me throughout my life. Without them, I would not be here today. To my supervisor, Dr. Louis Mercier - thank you for giving me the opportunity to work and learn from you for the past three years. My past and present coworkers, Mauricio Melo and Babak Fotoohi, have helped me so much along the way, and I thank them as well. Also, Dr. William Zhe, who graciously prepared and analysed samples for me, deserves my gratitude. Finally, I want to thank the staff and faculty in the Department of Chemistry and Biochemistry at Laurentian University for allowing me to pursue my degrees.

I wish to bid Laurentian University a fond farewell, for it has given me the six greatest years of my life. I will truly cherish the memories.

Table of Contents

List of Figures

List of Tables

1. Introduction

1.1 Natural Silicate Minerals

Silicate minerals are naturally-formed rocks containing the silicate anion, SiO_4^{4-}. Natural silicate minerals, such as zeolites, have been studied and used for different applications over many years because of their unique framework structure. Zeolites are aluminosilicate minerals, and are just one of several groups of minerals with a framework structure. By definition, zeolites are three-dimensional "tecto-silicates" (also known as framework silicates) composed of covalently linked SiO_4 and AlO_4 tetrahedra through their oxygen atoms. The resulting structures contain interconnected cages and channels that posses a net negative charge due to the substituted Al^{3+} within the framework of the zeolites.[1] The resulting local charge, along with its microporous structure (pore sizes up to 20 Å) permits access for water which contains cations that balance the negatively charged framework. The pore sizes of zeolites are not only governed by the frameworks themselves, but also the size of the exchangeable cations present within the pore channels.[2] The presence of water molecules and exchangeable cations are what separates zeolites from all other framework silicates, and allows them to be employed for a number of different applications.[1]

Since the mid-20th century, zeolites have been used for applications in molecular sieves,[1-2] catalysis,[1,3] and ion-exchange.[1,4] The vast range of zeolites in existence provides a basis for molecular sieve applications. Zeolites are particularly useful as industrial catalysis, most notably in the petroleum industry. The structure, topology, and charge of zeolites induces selectivity which can be employed for isomerisation and cracking reactions, such as the formation of branched isomers from simple *n*-alkanes and

the cleavage of long chain hydrocarbons into smaller ones, respectively.[3] Furthermore, the ion-exchange capabilities of zeolites opens applications in adsorption for industrial and environmental remediation. Heavy metal ions,[4-5] along with other impurities such as ammonium ions,[5] are perhaps the most investigated contaminants in wastewater through adsorption via ion-exchange.

Clay minerals are another group of silicates that have been studied for applications in adsorption. These minerals are hydrous aluminosilicates, although they often contain variable amounts of other cations such as iron, magnesium, etc. They are generally defined as those minerals that compose the colloid fraction of soils, sediments, and water.[6] Like zeolites, clays possess high sorption capacities and negatively charged surfaces, which allows for ion exchange. Natural clays exhibit both Brønsted-Lowry and Lewis type acidity, ultimately affecting their adsorption capacity. The Brønsted acidity occurs from the presence protons on the surface of the clay, formed by the dissociation of water molecules of hydrated exchangeable metal cations. Conversely, Lewis acidity arises from exposed Al^{3+} at the edges or through the dehydroxylation of the Brønsted acid sites, resulting in rupture of Si-O-Al bonds.[7]

Classified as phyllosilicates, or sheet silicates, clays contain metal octahedra sheets, which are covalently linked through oxygen atoms to silicate tetrahedra sheets, forming layers that stack on top of one another. These stacks are better known as "lamellar" structures, held close by van der Waals interactions. The abundance of clays in nature make them attractive minerals for many applications in adsorption and catalysis. The minerals can also be modified in a number of ways to improve their adsorption

capacities. Whether clays are tailored or in their natural state, the low cost, abundance, and desirable properties make them very attractive adsorbents.[8]

The great abundance of zeolites, clays, and other natural silicates, and in particular tecto-silicates, has provided researches with a tremendous amount of materials that may be applied in various ways. Chemical modification techniques have been used to induce selectivity for even more applications. The porous nature of tecto-silicates, or framework silicates, that results in higher surface areas, is their distinguishable feature.

1.2 Synthetic Silicate Materials

As the need for better and more applicable materials increases, new classes of silicon-based materials are emerging. The tecto-silicate known as silicon dioxide, or silica, has been reproduced in the lab setting. In nature, silica exists as the mineral quartz, and is the main component in beach sand. Synthetic analogues of silicon dioxide are not new. For example, silica gel is porous, amorphous, and very hygroscopic, and has therefore been used as a desiccant for centuries. It has also been employed more recently as a stationary phase in column chromatography applications.[9]

1.2.1 Mesoporous Silica

In 1992, Beck *et al*. created a novel silica material which they called Mobil Composition of Matter No. 41, or MCM-41.[10] This silica gel-like material displayed a well-ordered framework, uniform pore size in the mesoporous range (≥20 Å), and extremely high surface area (≥1000 m^2/g).[10-11] This material, along with many variations produced since then, have come to be known as mesoporous silica. Mesoporous silicas are synthesized via a sol-gel process, involving the hydrolysis and condensation of silicon-based inorganic precursors around a micelle template (Figure 1.1). The template

is then removed by means of calcination or solvent extraction, and a three-dimensional network of uniform pore channels remains.[10-21] The micelle template consists of self-assembled aggregates of amphiphilic surfactant molecules in water. The surfactant molecules are typically composed of a long-chain hydrocarbon tail attached to a hydrophilic head (typically charged). By controlling surfactant concentration, the shape and order of the formed micelles in an aqueous solvent can be tailored, which ultimately affects organization of the assembled mesostructures. While Beck *et al.* displayed a hexagonal-ordered material,[11] lamellar[12] and cubic[13] mesophases have also been identified in the MCM class of mesoporous silica, simply by adjusting surfactant concentration.

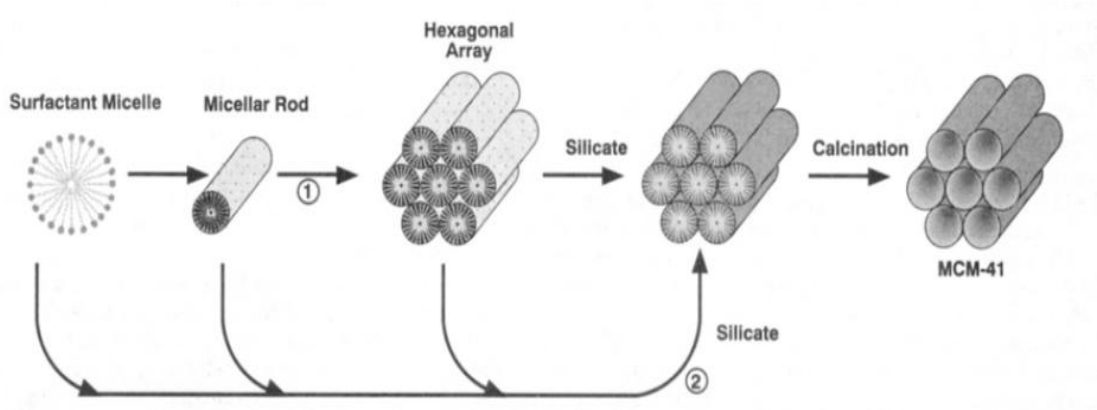

Figure 1.1 Mesoporous silica type MCM-41 assembly, taken from ref. [10]

A common and useful inorganic precursor for the synthesis of mesoporous silica is tetraethyl orthosilicate (TEOS). For MCM-41, the precursor is hydrolysed under basic conditions, which causes the formation of negatively charged species (I^-). The procedure requires a cationic surfactant (S^+) to achieve direct electrostatic assembly, resulting in an ionic interaction of charged species at the micelle-water interface (S^+I^-).[10-14] TEOS may

also be hydrolysed under acidic conditions, forming positively charged silicate species (I^+). An anionic surfactant (S^-) with a negatively charged head group would then be the ideal surfactant candidate. However, it has been shown that only disordered mesophases resulted from the use of anionic surfactants.[15] Instead, non-ionic block copolymers like Pluronic P123 have been adopted for the acidic synthesis of mesoporous silica, producing a material known as Santa Barbara Amorphous No. 15 (SBA-15). Block copolymers are made up of segments or "blocks" of different polymerized monomers. They have the advantage that their ordering properties can be adjusted by solvent composition, molecular weight, or copolymer architecture.[15] SBA-15 materials exhibit extremely large pore sizes with thicker walls than MCM-41, leading to increased hydrothermal stability.[14] The SBA-15 synthesis route proceeds with a balance of Coulombic, hydrogen bonding, and van der Waals interactions. Under acidic conditions (from HCl), the interaction between the block copolymer (N^0) and protonated silicate species (I^+) is designated as $(N^0H^+)(X^-I^+)$, where H^+ and X^- are protons and halide anions, respectively.[17]

Non-ionic block copolymers, along with neutral surfactants have also been used under neutral conditions to produce other types of mesoporous silica. Michigan State University (MSU) mesoporous silica has been prepared under such conditions via a N^0I^0 pathway, operating via hydrogen bonding.[18-19] Like MSU mesoporous silica, Hexagonal Mesoporous Silica (HMS) is prepared under neutral conditions, but the surfactant used is a neutral one (S^0), typically primary amines. Therefore, the synthetic pathway for HMS-type silica operates through an S^0I^0 mechanism.[20-21] Though the weaker hydrogen bonding provides thicker walls and high stability, both HMS and MSU mesoporous silicas exhibit spherical morphologies containing less-ordered, three-dimensional

"wormhole motif" porosity.[18-21] However, neutral amine surfactants used in the HMS-type silicas are toxic and costly, and therefore less ideal for synthesis.[17] The block copolymers possess an environmental advantage over most other surfactants due to their biodegradability.[19] A comparison of the four types of mesoporous silica can be seen in Figure 1.2:

	ELECTROSTATIC ASSEMBLY	**NON-ELECTROSTATIC ASSEMBLY**
TYPE	MCM-41 (S^+I^-) SBA-15 (N^0H^+)(X^-I^+)	MSU (N^0I^0) HMS (S^0I^0)
SURFACTANT	Quaternary alkylammonium halides Non-ionic surfactants	Non-ionic surfactants Primary amines
CONDITIONS	Alkaline or acidic Hydrothermal	Neutral pH Room temperature
SURFACTANT REMOVAL	Calcination (>600 °C)	Ethanol extraction
STRUCTURE	Ordered, hexagonal structure  Taken from ref [10]	Disordered, wormhole motif 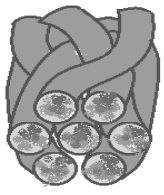
TEXTURAL PROPERTIES	Large, fibrous particles	Fine, spherical particles

Figure 1.2 Comparison of mesoporous silica assembly mechanisms

1.2.2 Functionalization of Mesoporous Silica

Research in the field of mesoporous silica has led to the widespread practice of organic functionalization. Incorporation of chemically reactive organic moieties into the robust inorganic silica framework is of significant interest and has led to increased applicability of these materials because they are more tunable for various sorption studies. Organofunctionalization is carried out using specific coupling reagents known as organosilanes. These compounds are similar to the purely inorganic precursor TEOS, in which the tetravalent silicon is primarily surrounded by alkoxy groups. However they typically contain branched, non-hydrolysable organic groups from the central silicon atom. Functional groups such as thiols, amines, carboxyl groups, and many others are attached to what is usually an alkyl chain as the branched moiety.

Immobilization of organosilane coupling reagents onto the mesostructure (also known as silylation) can be accomplished by two different methods: Post-synthesis grafting and co-condensation. Grafting refers to the modification of the surface of the already-synthesized mesoporous silica. Silylation occurs on silanol groups that exist on the surface of the materials, and therefore surface coverage by organic groups is contingent on the number of sites available.[21-23] The grafting process is carried out in an organic solvent (usually toluene), where it is imperative that the pre-synthesized material is dried completely to avoid self-condensation of the organosilane.[22,24-25] The other method of functionalization, known as co-condensation, is a one-pot synthesis technique, in which the organosilane is combined with TEOS at a specific ratio. This process produces a material with a controlled amount and homogeneous distribution of organic groups on the surface:

$$Si(OEt)_4 + R_nSi(OR')_{4-n} + (8-n)H_2O \rightarrow Si(OH)_4 + R_nSi(OH)_{4-n} + (8-n)R'OH \quad (1)$$

$$Si(OH)_4 + R_nSi(OH)_{4-n} \rightarrow (OH)_3Si\text{-}O\text{-}SiR_n(OH)_{3-n} + H_2O \quad (2)$$

The co-condensation method provides a high-quality material at a decreased cost. Organosilane usage can be controlled, and the surfactant is no longer consumed because it is extracted by a solvent (organic moieties would burn off during calcination).[23] Drawbacks to this method occur when attempting to increase the organosilane content above 20%, which leads to disordered mesopores.[24] An illustration of the methods of organofunctionalization of mesoporous silica can be seen in Figure 1.3. It can be seen that a third approach to the organic functionalization of mesoporous silica is available. This method utilizes the co-condensation procedure as previously mentioned, however the organosilanes that are used are different.

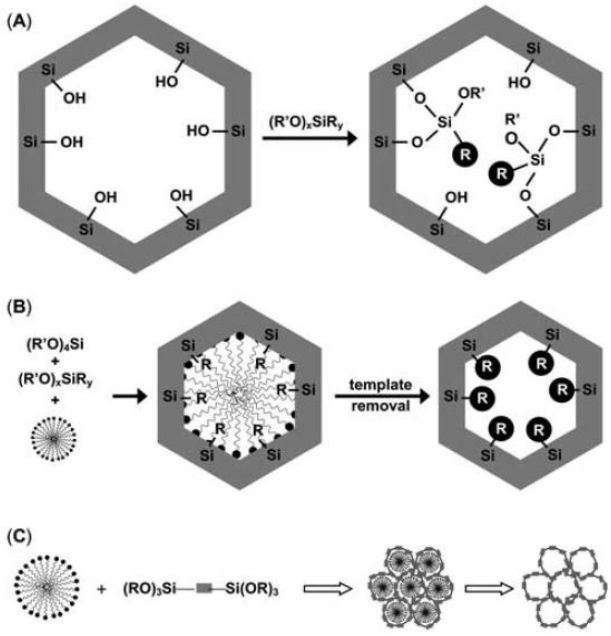

Figure 1.3 Methods of organofunctionalization of mesoporous Silica by (a) post-synthesis grafting, (b) co-condensation, and (c) framework incorporation, taken from ref. [24]

By utilizing bridged or "bis" organosilanes, the condensation results in a material with an organically modified framework, as shown in Figure 1.3c. This "chemistry inside the walls" approach allows the mesoporous materials to be synthesized purely with organosilane, rather than in a mixture with inorganic precursor. As opposed to grafting and traditional co-condensation, framework incorporation provides relatively unimpeded pore channels. However, structural problems arise when using long-chain bis-silanes, as organic groups are less rigid than the inorganic framework. Thus, pore collapse is inevitable when the framework mainly consists of organic chains.[24, 26-27]

1.2.3 Synthetic Organoclays

Like mesoporous silica, clay materials have been increasingly studied in the last few decades, albeit to a lesser extent. Clays are similar to mesoporous silica in their porous nature along with their high surface areas. Organic functionalization of clays is possible through the utilization of organosilane reagents. However, they are not classified as the same types of silicates as mesoporous silica (or silica in general). Clays are phyllosilicate materials, typically hydrous aluminosilicates, but often containing variable amounts of magnesium, iron, and other cationic metals.[28]

Hydroxyl groups are known to exist on the edges of clay particles, but structural defects and irregularities may cause them to be located in the interlayer regions. These groups, like mesoporous silica, are the available sites for the grafting of organosilane coupling reagents.[29] Pillared clays like montmorillonite have been used in this grafting process, however it is suggested that the micropores of these natural clays could be clogged by the grafted functional groups.[30] In response, synthetic routes established from the synthesis procedure of mesoporous silica have been used in this area of research.

Like mesoporous silica, it has been discovered that surfactants can be used to expand the pore sizes of the phyllosilicates into the mesoporous range. Porous clay heterostructures (PCHs) are prepared by the self assembly of a silica source around surfactant micelles (embedded by ion exchange) between the layers of the phyllosilicate. Rather than a three-dimensional construction of framework silica, it is assembled in two dimensions, as dictated by the phyllosilicate host. The surfactant is then removed by calcination or solvent extraction, and a stable PCH is produced (Figure 1.4).[31] This process also introduces more hydroxyl sites to the interlayer regions of the phyllosilicates, allowing for higher degrees of functionalization.[30-32]

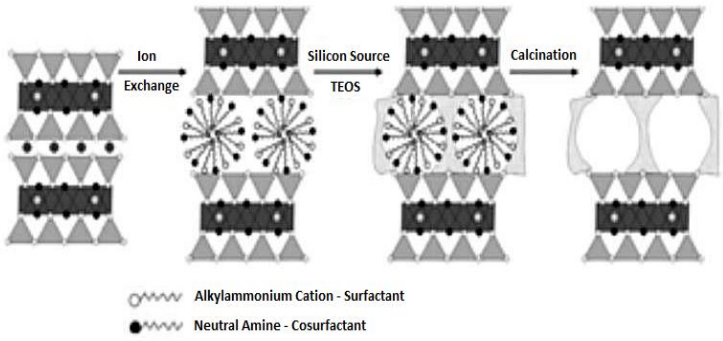

Figure 1.4 Preparation of porous clay heterostructure, taken from ref. [31]

Self-assembled clay hybrids based on a sol-gel process at room temperature have gained more attention due to the soft synthetic approach. The formation of lamellae through direct covalent bonds has been shown to produce well-ordered materials. Adding silicon precursors to divalent metal cation (magnesium or nickel) salts at alkaline pH values induces the formation of linked silicate tetrahedra and metal octahedra sheets. The

metal ions in solution form insoluble hydroxides under basic conditions, forming the octahedra layer. A silicon source is then added, which hydrolyses and condenses to form the tedrahedra layer. Furthermore, the procedure allows the formed sheets to connect through Si-O-M bonds (M = Mg, Ni).[33-34] Controlling the silicon-to-metal ratio is critical for the formation of specific phyllosilicates, and classified in the 1:1 or 2:1 family.[35] For example, a Si/Mg molar ratio equal to 4/3 produces a material that resembles the ideal formula for talc, a 2:1 trioctahedral phyllosilicate, $Mg_3Si_4O_{10}(OH)_2$. The structure of talc and other 2:1 phyllosilicates can be pictured as a layer of magnesium oxide octahedra sheets sandwiched between two silicate tetrahedra sheets. A synthetic material such as this one possesses advantages over natural talc, because it has special properties like high purity, homogeneity, and controlled porosity.[36]

Synthetic phyllosilicates are attractive materials for introducing functional groups in between the layers. A common name given to these types of materials is "organoclay." Incorporation of organic species into inorganic layers was first explored by Ukrainczyk *et al*.[36] Further projects utilized this procedure with multiple organic moieties (various organosilanes) to increase the applicability of the organoclays.[37-39] Organosilane coupling reagents may be used as the sole silicon precursor in the synthesis of organoclays, which increases chemical reactivity. The sol-gel process enables the organosilanes to form tetrahedral sheets and cross-link to the given metal octahedra. Organic groups originating from the silylating agents are therefore intercalated and covalently bonded to the inorganic layers (Figure 1.5). Therefore, the interlayer spacing of the phyllosilicate directly corrrelates to the length of the organic chain. The lamellar stacking of the phyllosilicates is also influenced by the van der Waals interactions

between the organic moieties.[33-39] A schematic diagram of the synthesis of the organoclay hybrids is illustrated in Figure 1.6.

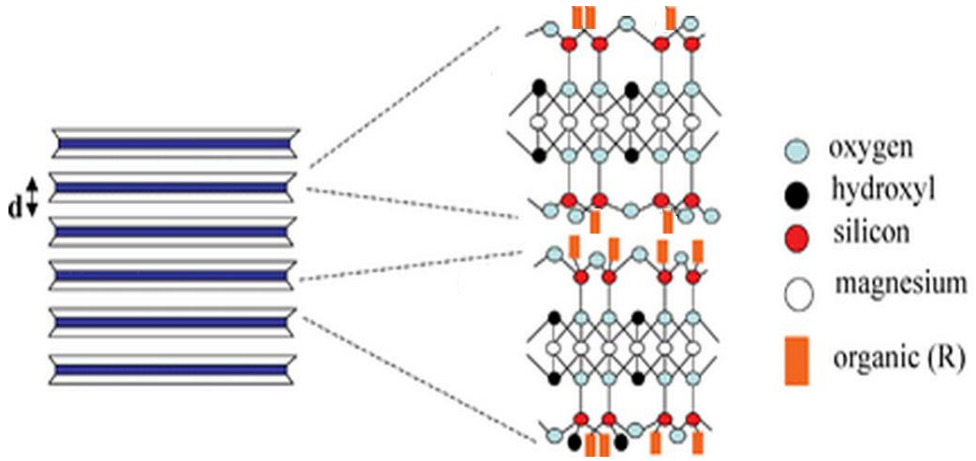

Figure 1.5 Two-dimensional representation of talc-like organoclay, adapted from ref. [40]

Organoclays offer a number of advantages over other silicon-based materials in terms of functionalization. As mentioned previously, mesoporous silica possesses limitations in this aspect. Co-condensation of organosilane and inorganic precursor allowed for homogeneity and controlled amounts of functional groups. However, structural failure results when too many organic groups are introduced. This problem is eliminated in organoclays, because the rigid metal silicate layer provides a solid backbone to which the organic chains can anchor. Although the use of 100% organosilane is possible in the synthesis of PMOs, long-chain organic moieties cannot support the framework of the mesostructures. For organoclays, the structure and the process allows for both short-chain[33-37, 39-40] and long-chain[38,41] organic groups to be formed within the phyllosilicate layers. Aside from function, organoclays do not require a surfactant template, so the synthesis procedure is more cost-effective.

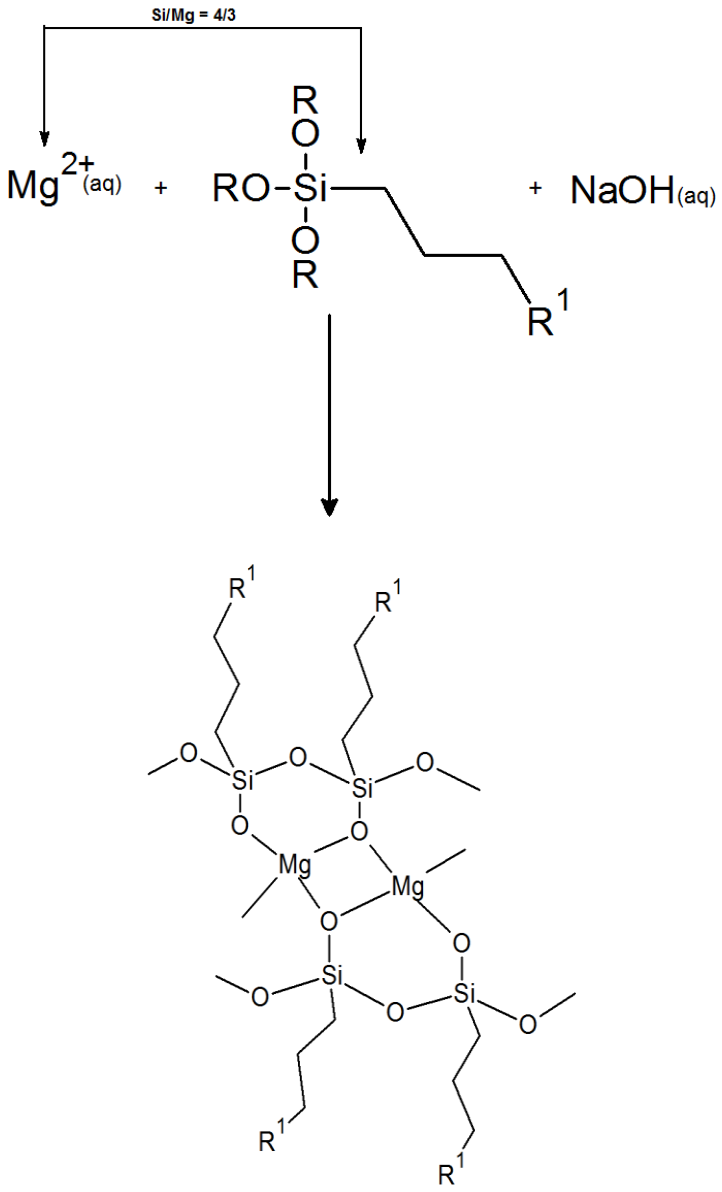

Figure 1.6 Synthesis of organoclay hybrid

1.3 Applications in Metal Ion Adsorption

The functionalization of silicon-based materials tremendously increases their applicability. Reactive organic groups branched from the surface opens up applications in catalysis,[14,22,24,42-43] drug delivery,[24,44-45] and adsorption.[22-31,45] Adsorption of chemical species, either organic or inorganic, is of great importance in the field of environmental

and industrial remediation. The added selectivity introduced upon functionalization causes the materials to exhibit higher adsorption capacities relative to natural mineral and purely inorganic structures.

1.3.1 Heavy Metal Pollution

Pollution of lakes, rivers, and oceans by heavy metals is a major concern in today's world, especially in developing countries. Increasing metal ion concentrations in water resources not only affects the water supply, but also the quality of life in humans, plants, and animals. Unlike organic compounds, heavy metal ions are non-biodegradable, and their widespread use has made them ubiquitous in the environment. Copper is found in many industries, including electronics, mining, metal plating, plumbing, and others.[46] It is an essential trace element for humans, but it becomes toxic in large amounts, and there is evidence to suggest that copper may be carcinogenic.[47] Another heavy metal pollutant that is a known carcinogen is nickel. Widely used in silver refineries, electroplating, and battery industries, nickel's toxicity is well-known. Though it is an essential element in trace amounts, in particular for plant growth,[48] nickel causes is a known carcinogen.[49] Other elements, such as lead, are toxic to plants and animals at all levels, even trace amounts. The health effects of lead have been known for many decades. It accumulates in the bones, brain, kidneys, and muscles, leading to serious mental disorders, cancer, and coma.[50] Measures have been taken to decrease lead emissions into the environment through government legislation and public awareness. However, it is a very useful metal in industry, so it is still widely applied to this day. Batteries, paint, printing, dyes all employ lead in their respective industries, so it is

necessary to clean up their waste, and adsorption by silicate materials may be an ideal approach.[50-51]

1.3.2 Adsorption of Heavy Metal Ions by Silicate Materials

Adsorption is one of the simplest, most effective, and inexpensive approaches for environmental remediation. One of the most widely used adsorbent in the world is activated carbon, which is used to trap multiple types of pollutants, including heavy metals. Adsorption of heavy metals by activated carbon is accomplished by non-selective uptake. Functionalized silicon-based materials possess reactive organic groups which add selectivity towards specific types of ions. The reactivity of chosen functional groups towards specific metal ions is typically dictated by the hard-soft lewis acid-base (HSAB) theory. For example, many synthetic silicates have been functionalized with thiol groups (a soft lewis base) for effective mercury ion (a soft lewis acid) adsorption.[22-25,29-30,32] Other organic moieties such as amines,[24,36,52-54] carboxyls,[24,34-35] halides,[24,35,39] and others have been immobilized on the silicate surfaces for the adsorption of a variety of metals. Amines are particularly useful in the adsorption of many heavy metals, including copper, nickel, and lead. Amines as a part of chelating agents, such as ethylenediamine (*en*), can be incorporated into silicate materials for improved adsorption as well.[52-53]

1.3.3 Ion-Imprinting for Induced Specificity

An emerging technique for improving adsorption of heavy metal ions from aqueous solutions is the ion-imprinting method. In silicon-based materials, ion-imprinting involves the complexation of a metal ion with the functional groups of the organosilane prior to synthesis of the adsorbent itself. Removal of the imprinted ion from the final structure results in specific recognition sites, complementary to the ion in terms

of shape, size, and functionality in the material. The goal of this technique is to achieve higher selectivity and affinity towards a specific metal ion, and in a sense bypassing formation constants. Such specificity is attractive in multivalent systems, like most water resources in the world. This method has already been employed on mesoporous silica, using both amine,[53] and ethylenediamine ligands[54] (Figure 1.7). Though these imprinted sorbents showed higher selectivity and capacities in the adsorption of copper(II) ions over zinc(II),[53-54] the nature of the ligands leaves room for improvement. Branched amine or ethylenediamine moieties within the pore channels of mesoporous silica are still flexible after complexation and removal of the ion template. There is no "anchor" for these functional groups on the surface of the material.

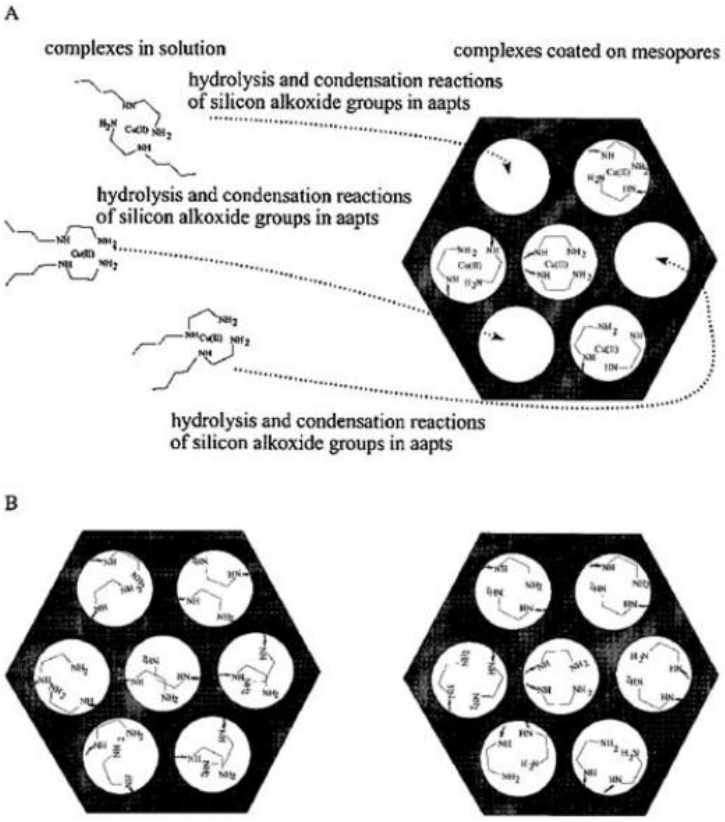

Figure 1.7 (a) Schematic diagram of the copper(II) ion-imprinting process of mesoporous silica with ethylenediamine moieties and (b) the difference between conventional grafting (left) and imprinting (right), taken from ref. [54]

Using a bridged organosilane appears to be a suitable response to this problem, but as mentioned in a previous section, there are restrictions on the amount and organic chain length of the organosilane that may be used. In order to bypass these common issues associated with mesoporous silica, an alternative silicon-based hybrid must be employed. Clay materials are an attractive candidate for this purpose, as they can accommodate a higher loading and a broader range of organosilane precursors.

1.4 Objective

This thesis project will focus on the synthesis, characterization, and some adsorption applications of organoclay hybrids. A talc-like magnesium phyllosilicate was chosen as the material due to its relatively simple formula, $Mg_3Si_4O_{10}(OH)_2$. A soft sol-gel synthetic approach for preparing this material will be used as it is both simple and effective. The material will then be used to study the adsorption of copper, nickel, and lead, since these metals are found in industrial waste, and have adverse effects on the environment. Amine ligands have shown to be extremely effective in adsorption of these metal ions.[24,36,52-54] Due to the nature of the clay material itself, immobilization of a large number of organic functional groups should be permitted. The ethylenediamine moiety will be introduced to the structures, as it is a known chelating agent for all three metals. Because it is a relatively long organic chain, a rigid structure is required, and the talc-like phyllosilicate material seems to be the ideal host material for the ethylenediamine ligand.

Ethylenediamine organosilane coupling reagents exist both as single branched silanes, and bridged "bis"-silanes. In either case, it is unnecessary to combine the organosilane with a purely inorganic precursor like TEOS. The use of the bis-*en*

organosilane has been previously studied by Mercier, *et al.*[52] in the production of ethylenediamine-functionalized PMOs. Although the material was an effective metal ion adsorbent, *en* loadings were only possible up to 5% to maintain structural integrity.[52] Phyllosilicates contain a rigid backbone that will not allow structural damage upon functionalization with a large amount of long-chain organic groups. Therefore, the silicon tetrahedra sheets formed will consist of 100% organosilane precursor, and ultimately higher organic content. Bridged ethylenediamine organoclay hybrids will be synthesized and compared in this project. Effects of interlayer spacing, lamellar stacking, and overall structure will also be studied.

The ion-imprinting procedure will also be investigated with this type of material. This project aims to produce an organoclay functionalized with bridged organosilane precursors to provide support for a metal ion-template. By essentially providing a non-flexible organic moiety for the structure, adsorption capacities and specificity should be easily tunable.

2. Experimental

2.1 Synthesis and Characterization of Ethylenediamine-Functionalized Organoclay

2.1.1 Materials

The bridged organosilane, *N*, *N'*-bis[3-(trimethoxysilyl)propyl]-ethylenediamine (BTMDA - 62% in methanol) was purchased from Gelest Inc. Magnesium nitrate hexahydrate, $Mg(NO_3)_2 \bullet 6H_2O$ (98%), was used as the magnesium source and was obtained from Alfa Aesar. The synthesis also required sodium hydroxide, which was purchased from Sigma-Aldrich (pellets, $\geq$ 97%). For the adsorption assays and the ion-imprinting procedure, nitrate salts of copper (J. T. Baker Chemical Co.), nickel (BDH Chemicals Ltd.), and lead (BDH) were purchased and employed. For the adsorption tests, standard solutions for each metal ion (1000 ppm - 3% HNO_3) were used and obtained from Sigma-Aldrich.

2.1.2 Synthesis of MgSi-b-en

The organoclay was synthesized from a mixture of magnesium nitrate and the silylating agent. To a beaker containing 2.4038 g of $Mg(NO_3)_2$ dissolved in 25 mL of ethanol, another 25 mL ethanolic solution with 3.8772 g BTMDA was added and stirred at room temperature. The molar ratio of Si/Mg was calculated to be 4/3, in relation to the chemical formula for pure talc, $Mg_3Si_4O_{10}(OH)_2$. While stirring the solution, 62.5 mL of an aqueous solution of sodium hydroxide (0.2 M) was added dropwise. A yellowish-coloured suspension was produced upon addition of the sodium hydroxide. The solution was left to stir for one hour, and was then transferred to a Teflon-lined autoclave where it was hydrothermally treated at 373 K for 24 hours. The resulting gel-like material was filtered and washed using a Soxhlet extractor containing ethanol to remove excess

magnesium. The solid, named MgSi-b-*en*, was then dried at 350 K for 48 hours. An illustration of the expected structure of the synthesized organoclay material, along with the molecular structure of the BTMDA precursor can be seen in Figure 2.1:

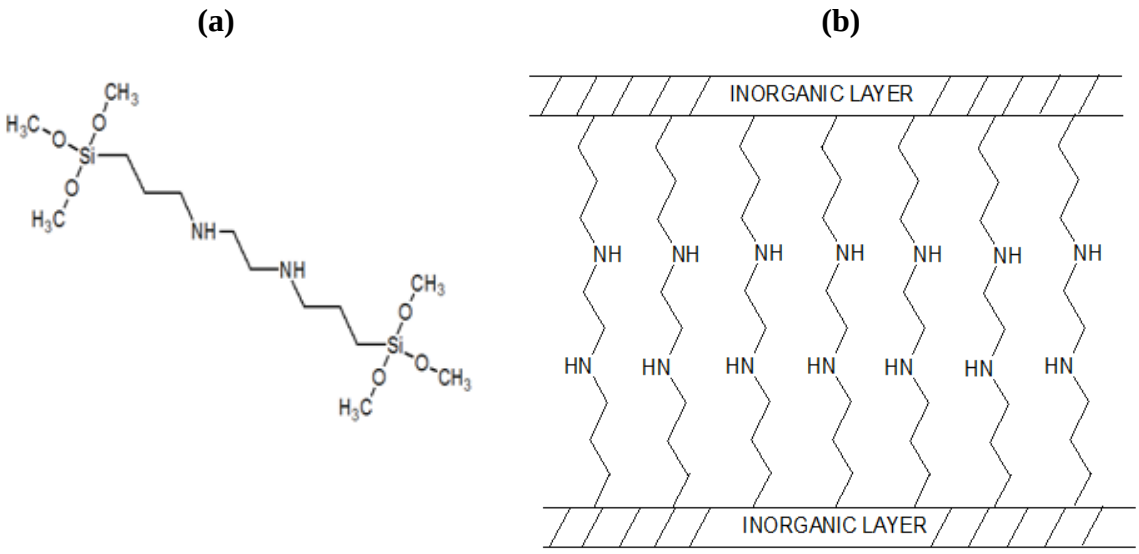

Figure 2.1 (a) BTMDA and (b) expected structure of MgSi-b-*en*

2.1.3 Characterization of MgSi-b-en

To analyse their structures and morphologies, the synthesized phyllosilicate materials were characterized using powder X-ray diffraction (XRD), nitrogen (N_2) adsorption isotherms, scanning electron microscopy coupled with energy-dispersive X-ray spectroscopy (SEM-EDS), infrared spectroscopy (IR), and thermogravimetric analysis (TGA).

2.1.3.1 X-ray Diffraction

XRD patterns were obtained with a XDS 2000 instrument from Scintag Inc. using Co K_α radiation (λ = 1.789 Å). The powder samples were immersed in a few drops of ethanol and spread onto a sample holder prior to analysis. After measurements were

taken, Bragg's law, $n\lambda = 2d\sin\theta$, was applied to the data, where n is an integer, λ is the wavelength of the incident X-rays on the material with an atomic lattice separated by distance d (d-spacing), and θ is the diffraction angle between the incident rays and lattice planes. Full spectrum scans of 2θ angles ranging from 5 to 75 degrees were performed. The d-spacing between the lattice planes of materials were to be determined by interpretation of the peaks in the resulting XRD spectra and application Bragg's law. XRD also reveals structural information of a material such as periodicity and overall crystallinity.

2.1.3.2 Nitrogen Adsorption Isotherms

On a Micromeritics ASAP 2010 system, roughly 0.1 g of material was degassed for at least 6 hours at 80 °C prior to analysis. N_2 adsorption isotherms of each sample were then measured at 77 K (-195 °C). The surface area was calculated from the isotherms using the Brunauer, Emmett, and Teller (BET) model,[55] the most widely used isotherm dealing with multilayer adsorption, expressed by the following equation:[56]

$$\frac{V}{V_{mon}} = \frac{cz}{(1-z)[1-(1-c)z]} \qquad \text{where} \qquad \mathbf{z} = \frac{\mathrm{P}}{\mathrm{P_0}} \tag{3}$$

In this expression, V_{mon} is the volume required to form a monolayer, c is a constant, and z is the relative pressure of adsorbed gas (P/P_0). The equation can also be re-written in the following form:[56]

$$\frac{z}{(1-z)V} = \frac{1}{c\times V_{mon}} + \frac{(c-1)z}{c\times V_{mon}} \tag{4}$$

Plotting the expression on the left side of the equation versus z makes it possible to determine the parameters V_{mon} and c. The surface area occupied by a single adsorbed N_2 molecule on the material's surface is estimated from the density of the condensed gas.

For N_2 at 77 K, that area is roughly 0.16 nm^2. Therefore, from the V_{mon} value obtained using the previous equation, the surface area of the material is calculated.[56]

The shape of the N_2 adsorption isotherm also reveals important information about the material. The BET model also describes five different isotherm types, based on their shapes. This ultimately correlates to the overall porosity exhibited by the material. Determination of pore size is dependent on the type of isotherm.

2.1.3.3 Scanning Electron Microscopy - Energy-Dispersive X-Ray Spectroscopy

SEM images were acquired using a JSM-6400 Scanning Microscope. Images were taken to analyse the structure and morphology of the materials. Samples were coated with a thin layer of carbon with a thickness of 15 nm and a density of 2.25 g/cm^3. The beam of electrons excites and ejects secondary electrons from the atoms on the surface of the material. These ejected electrons are detected to form an image of the surface of the material (a few nanometres deep), so the topography of the surface may be analysed, along with the size of the particles.[57]

The instrument was also coupled with an energy-dispersive X-ray spectrometer, which is useful for analysis and quantification of specific elements in the sample. During analysis, the incident beam of electrons may excite an electron from the inner shell of the atom. This creates an electron hole, which is immediately filled by an electron from the outer shell of the atom. An X-ray with an energy characteristic of the difference in energy between the two shells is then emitted by the transition. This characteristic X-ray is measured by the EDS detector that is equipped to the microscope. The results gathered

from this technique reveals information on the chemical composition of the surface of the material analysed.[57]

2.1.3.4 Infrared Spectroscopy

IR spectroscopy was performed on a Bruker Alpha Fourier Transform Infrared Spectrometer. All samples were dried and pressed into KBr pellets prior to analysis. Quantification of the organic groups was not possible using IR due to the absence of appropriate reference materials. However, IR spectroscopy was used to confirm the organofunctionalization of the hybrid structures. Other important details of the material structure, such as silica condensation were also revealed by IR spectroscopy.

2.1.3.5 Thermogravimetric Analysis

Like IR spectroscopy, TGA helps confirm the presence of organic moieties in a material. Analysis was performed on an SDT Q600 by TA Instruments against an α-alumina standard pan. Samples were heated at a rate of 10 K/min up to 1273 K in a nitrogen atmosphere. By measuring the weight loss of the material in relation to increasing temperature, data obtained from TGA was used to quantify the materials' organic content.

2.2 Heavy Metal Adsorption with MgSi-b-*en*

Cu(II), Ni(II), and Pb(II) nitrate salts were all used as heavy metal sources and dissolved in water. Adsorption parameters of pH, adsorbent dosage, contact time, and concentration were all analysed batch-wise. The tests of concentration were performed to produce adsorption isotherms for each system. Work used a single batch of adsorbent for all adsorption studies. All metal ion concentrations were tested against prepared standard

solutions. Quantitative analysis was performed on an AAnalyst 400 flame atomic absorption spectrometer (AAS).

2.2.1 Effect of pH

In order to determine an optimal pH for the adsorption of each heavy metal species, solutions with a range of pH values were prepared containing roughly 100 mg/L (ppm) of each metal ion. The pH of each solution was adjusted using dilute nitric acid and sodium hydroxide. The concentration of 100 ppm was chosen to ensure that the adsorbent would achieve saturation of chelating groups (calculated number of *en* groups via TGA). 5 mg of MgSi-b-*en* was placed into an Erlenmeyer flask containing 25 mL of solution, and put in a shaker over night. The solutions were then filtered and diluted accordingly, then analysed using flame AAS.

2.2.2 Effect of Adsorbent Dosage

The effect of adsorbent dosage was tested for each metal at the chosen optimal pH (determined from previous test). Batch adsorption methods were again used, as various amounts of the adsorbent, MgSi-b-*en*, were placed in 25 mL volumes of 100 ppm solutions of each metal salt, again to ensure saturation of the *en* active sites. After overnight shaking, the solutions were filtered, diluted, and measured by flame AAS. Dosage (reported in mg/mL) was tested against percentage removal along with adsorption capacity of the adsorbent.

2.2.3 Effect of Contact Time

100 ppm solutions of each metal were prepared to test the effect of contact time for the adsorbent. 25 mL of the solutions were poured into flasks containing the optimum pH and amount of material (established in steps *2.2.1 and 2.2.2*). Each flask was then left

to shake for designated periods of time ranging from 30 seconds to 24 hours before being filtered and diluted. After measuring metal ion content by flame AAS, the data obtained was fit to multiple kinetic models of adsorption.

To gain an understanding of the adsorption kinetics, it is necessary to fit the contact time data to one or multiple kinetic models. Kinetic models are significant because they provide knowledge of reaction pathways and mechanisms of adsorption. It is important to predict the rate at which pollutants are removed from aqueous solution for engineering purposes.[58] Recently, a pseudo-second order rate equation (PSOE) has been used to describe the adsorption of divalent metal ions from aqueous solutions:

$$\frac{dq_t}{dt} = k(q_e - q_t)^2 \quad (5)$$

Where, q_e and q_t are the sorption capacity at equilibrium and at time t, respectively, and k is the rate constant of pseudo-second order adsorption.[59-60] If the model holds true, the plot of t/q_t versus t should render a linear plot. It is often seen in these sorption processes that typical kinetic models are unsatisfactory in describing the rate of adsorption. The pseudo-second order model operates by the assumption that the rate-limiting step is governed by chemical adsorption through the active *en* sites and the metal ions on the surface of the material, rather than diffusion into the pores.[59] However, the kinetics are cannot be described by typical first or second-order models, and only fits the PSOE on the basis of the rendered linear plot.

2.2.4 Adsorption Isotherm

Using optimal pH, dosage, and contact time, solutions of metal salts at various concentrations were prepared and the sorption data was fit to an adsorption isotherm. The amount of remaining metal ions at each concentration (equilibrium concentration)

was measured once again by flame AAS. Isotherms for each metal ion were generated by plotting the amount of metal ion adsorbed per gram of material versus the equilibrium metal concentration. Adsorption models, like kinetic models, are valuable tools to describe the retention and mechanisms of adsorbed species onto porous solids.[61] Adsorption of divalent metal cations is often described by the Langmuir adsorption isotherm. This model operates on a number of assumptions, including monolayer coverage and homogeneous adsorption onto a finite number of equivalent active sites. Graphically, the Langmuir isotherm is a simple plot, in which a plateau occurs due to saturation of the active sites via chemisorption.

Other isotherm models have accurately described the adsorption mechanisms of multiple systems. The Freundlich adsorption isotherm is another simple model, which deviates considerably from the Langmuir model. The Freundlich isotherm addresses limitations in the Langmuir model, supporting multilayer and heterogeneous adsorption.[61]

2.2.5 Multi-Component Adsorption

Binary systems of Cu/Ni, Cu/Pb, and Ni/Pb were prepared with varying concentrations to examine the specificity exhibited by the adsorbent material. Concentrations at varying degrees of capacity were examined using normalized metal concentrations at levels of under-capacity, at-capacity, and over-capacity for each system. Each degree of capacity was determined by calculating the amount of *en* ligands in the organoclay using TGA, which can be related to the expected adsorption capacity. The optimal pH, dosage, and contact time used in construction of the adsorption isotherms were also used in these assays. All batches were measured in triplicate to determine the reproducibility of the system.

2.3 Metal Ion-Imprinting

Though MgSi-b-*en* exhibits a level of specificity based on the complexation constants for each metal ion and the ethylenediamine ligand, an imprinting method was adopted to alter the specificity. The synthesis procedure was similar to the original synthesis of MgSi-b-*en*, however one of three nitrates (Cu, Ni, Pb) was added to the reaction mixture. Prior to combining the organosilane precursor and the magnesium source, the metal ion salt was added at a specific ratio of *en* ligands to metal ion. Therefore, for every 2 moles of *en* added to the material, 1 mole of the chosen metal ion was combined (Figure 2.2). Confirmation of complexation was easily seen by a change in colour of the precursor, and upon basic hydrolysis, the resulting material maintained that colour. The imprinted adsorbents were then washed in ethanol to remove impurities and excess metals. Finally the bound ions were stripped from the material using 0.2 M ethylenediamine solution under reflux and then dried. The loaded and stripped materials were denoted MgSi-b-*en*(+M) and MgSi-b-*en*(-M) (M = Cu, Ni, Pb), respectively. All adsorbents prepared in this procedure were subjected to the same characterization techniques as the parent material (see *2.1.3 Characterization of MgSi-b-en*). Along with these techniques, each material was washed in a 5M HCl solution and the filtrate was subsequently analysed by Flame AAS to determine the efficacy of the *en* solution under reflux stripping method. Finally, binary metal systems containing Cu(II), Ni(II), and Pb(II) were prepared for selective adsorption studies (see *2.2.5 Multi-Component Adsorption*). Again, the replicates were performed on a single batch of adsorbent.

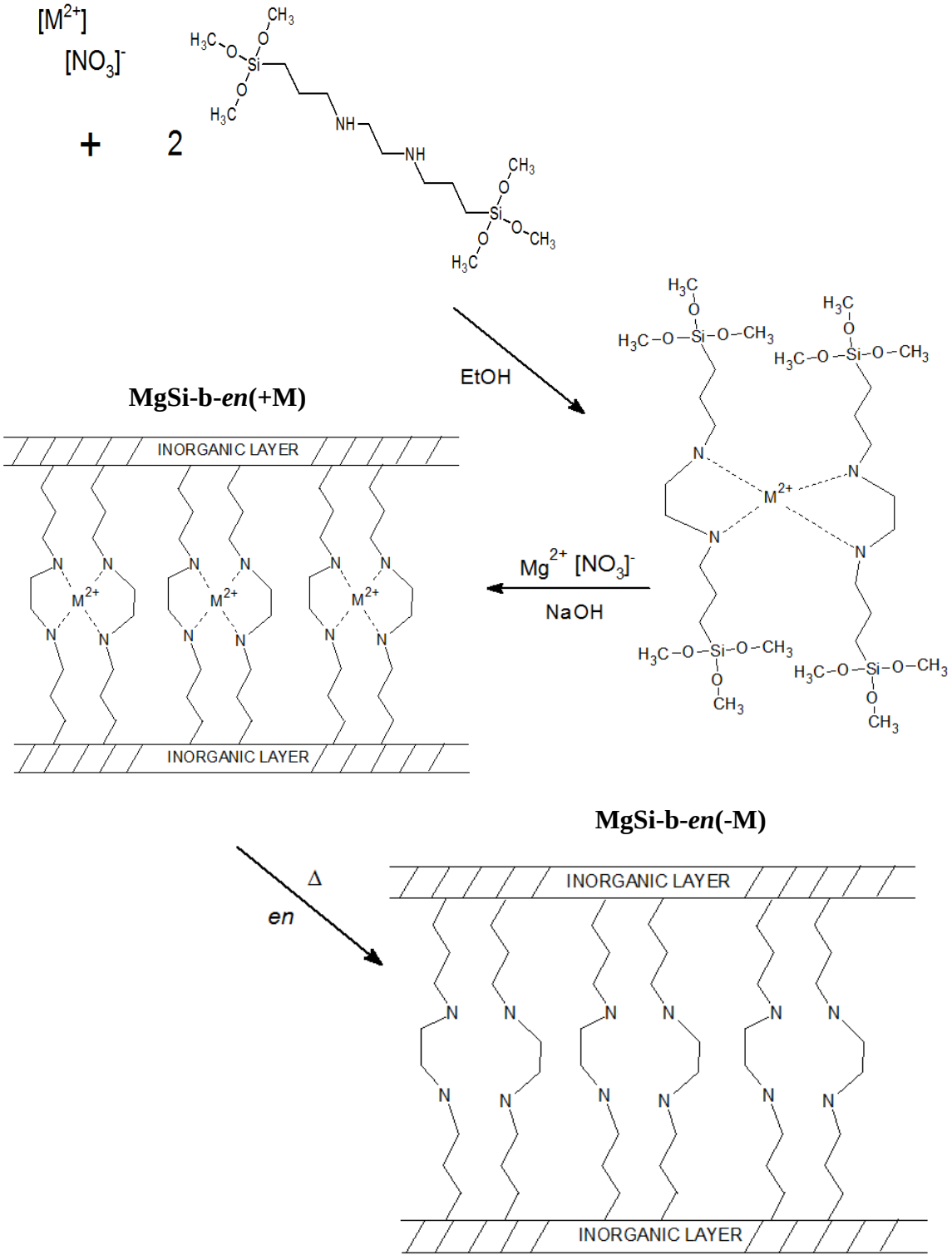

Figure 2.2 Synthesis of metal ion-imprinted adsorbent

3. Results and Discussion

3.1 Synthesis and Characterization of MgSi-b-*en*

3.1.1 X-Ray Diffraction

After grinding, the product designated MgSi-b-*en* existed in the form of a fine yellow powder. Figure 3.1 shows the XRD pattern of the material along with the pattern of natural talc (University of Arizona Mineral Museum 10563). Though the synthetic organoclay only exhibited a small degree of crystallinity, with diffraction peaks still resemble a talc-like substance.[34-41] However, the usual peak near $2\theta = 10°$ corresponding to the 001 reflection plane of natural talc was not visible in the XRD spectrum. The other peaks typically classified with mineral talc were present, but they were broad and of low intensity. This indicates a significant level of disorder within the structure of MgSi-b-*en*.

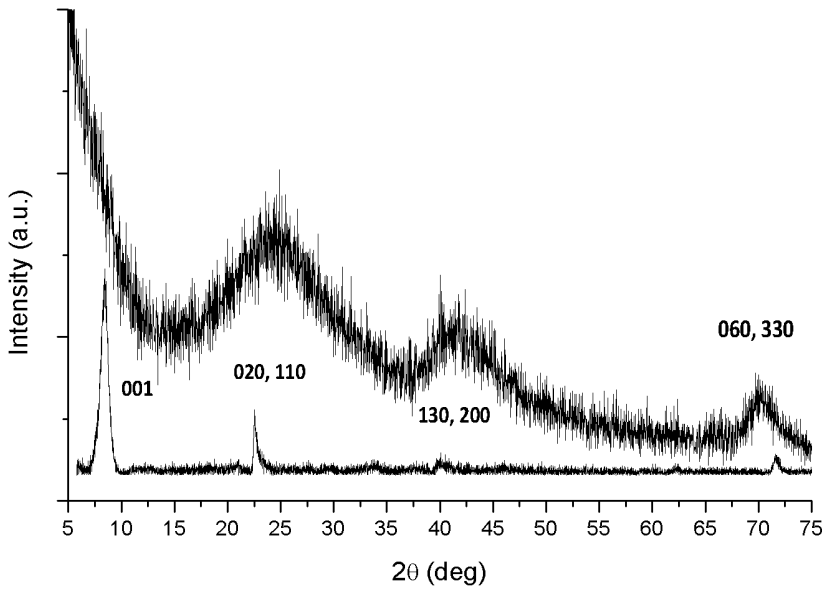

Figure 3.1 XRD patterns of MgSi-b-*en* and natural talc

The absence of the 001 reflection plane suggests that the lamellar stacking of the magnesium phyllosilicate layers did not occur during synthesis. Therefore, it is not possible to apply Bragg's law ($n\lambda = 2d\sin\theta$) to determine the d-spacing of the organoclay. Further structural characterization methods (namely SEM) would confirm the absence of lamellae in the material, which may be attributed to the use of the bis-silane used in the synthesis. Though this important peak is missing, other in-plane reflection peaks characteristic of talc are visible in the spectrum. The less intense but distinct peak at $2\theta=70°$, corresponding to the 060 reflection plane, is in agreement with the formation of trioctahedral layers.[35] Though these layers were produced, the data suggests that the overall structure formed clusters of sheets instead of lamellae.

3.1.2 Nitrogen Adsorption Isotherm

The N_2 adsorption isotherm of the parent compound, MgSi-b-*en* (Figure 3.2), displays type II behavior with a hysteresis, which normally indicates the presence of mesopores .[62] This is not expected from the material itself, however interparticle mesoporosity must be considered. The type II isotherm shows a large deviation from the Langmuir isotherm. As indicated by the isotherm, a monolayer is formed by the adsorption of gas molecules on the surface, followed by the formation of a multilayer. The increased adsorption past a monolayer is only possible on non-porous solids or within large pores (larger than micropores) capable of accommodating a multilayer. Such mesoporosity could be the result of the bridged organosilane precursor that may have also eliminated the lamellar stacking of the inorganic layers. Therefore, the bridging organic chain may not have induced microporosity between synthesized lamellae, but rather mesoporosity between the connected inorganic fibres. The BET model was then used to

calculate the surface area of the organoclay hybrid, which was found to be 531 m^2/g. The suspected morphology of the material is consistent with the high surface area - that is, a cluster of magnesium phyllosilicates induced by the bridged organosilane.

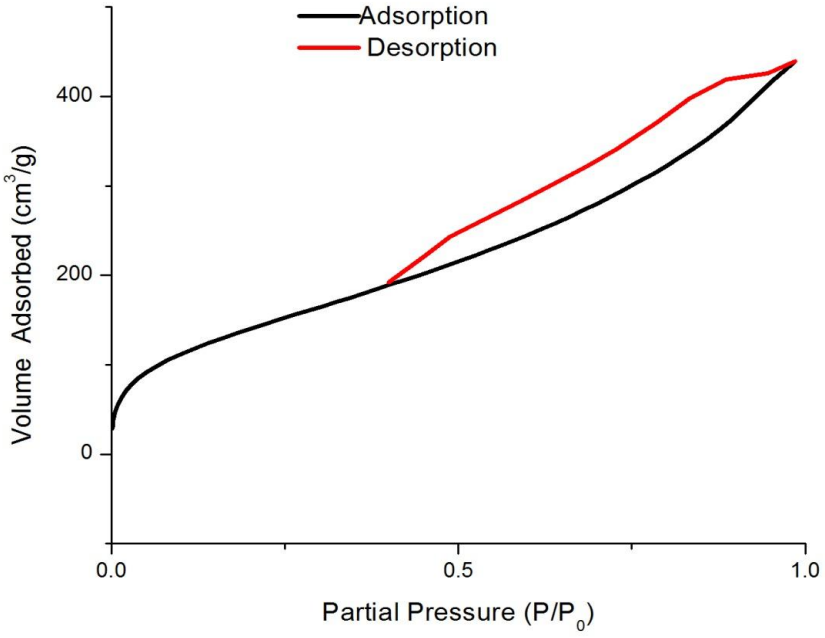

Figure 3.2 Nitrogen Adsorption Isotherm of MgSi-b-*en*

3.1.3 Scanning Electron Microscopy - Energy-Dispersive X-Ray Spectroscopy

SEM images of MgSi-b-*en* (Figure 3.3) revealed the expected morphology based on the XRD and N_2 isotherm results. Although magnesium-silicate layers were formed in the synthesis of the organoclay, these sheets did not exhibit the typical talc-like lamellar arrangement. Rather, a disordered conglomerate of interconnected phyllosilicate sheets was observed, although stacking did occur in the form of sheet overlap. The formed plates were irregularly-shaped and roughly 100 μm in diameter, although many of the sheets were smaller. The images (a, b, c - lower, medium, higher magnification,

respectively) are in agreement with the prior characterization results, as connected layers produce high surface area and disordered "mesopores" arise between them.

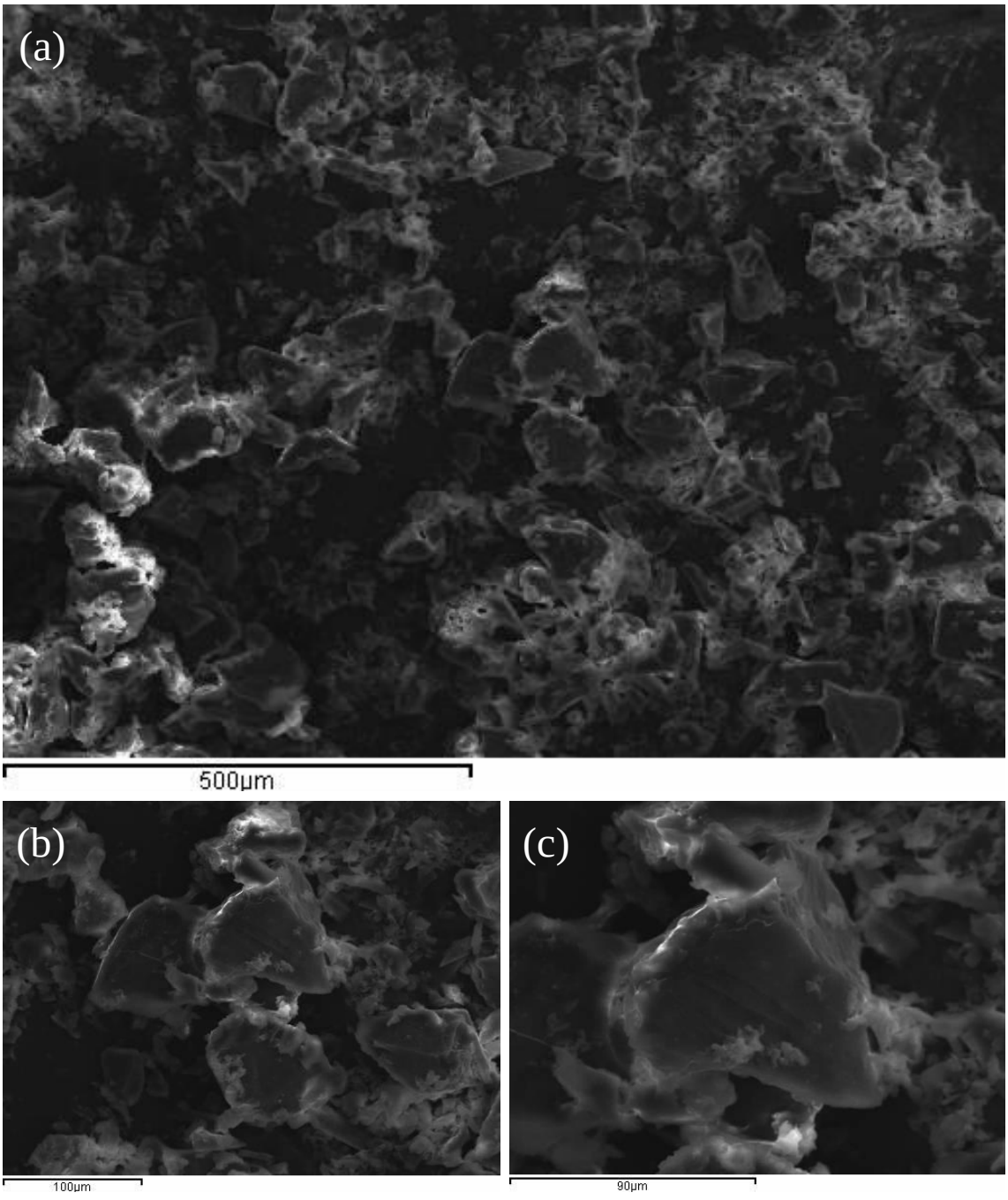

Figure 3.3 SEM Images of MgSi-b-*en*

Furthermore, results gathered from EDS indicated that the phyllosilicate sheets contained roughly 21% Mg, 31% Si, and 48% O, which is very similar to the chemical composition of natural talc (19.23% - Mg; 29.62% - Si; 50.62% - O). This confirms that the talc-like material, although disordered, was successfully synthesized, and is in congruence with the XRD pattern. The EDS spectrum (Figure 3.4) also reveals a small peak relating to the energy of nitrogen from amino groups. However, its signal is very faint, as amino groups are far less prevalent than other elements in the overall structure.

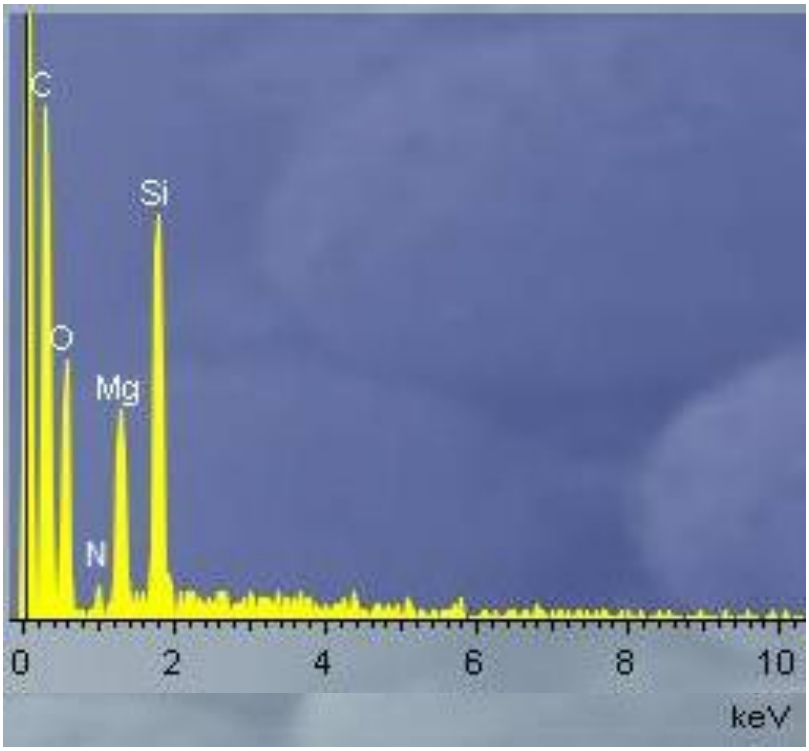

Figure 3.4 EDS Spectrum of MgSi-b-*en*

3.1.4 Infrared Spectroscopy

The IR spectrum of MgSi-b-*en* (Figure 3.5) revealed a broad absorption band centred around 3440 cm^{-1}, confirming the presence of -OH groups in the material. These terminal hydroxyl groups are typical functionalities of talc-like organoclays, as they arise from uncondensed silicate tetrahedra and magnesium oxide octahedra. The high intensity of this band may also be attributed to the presence of interstitial water molecules in the material. The less-pronounced band around 3800 cm^{-1} correlates to the MgO-H stretching vibration, which further agrees with the typical structure of the synthetic phyllosilicate. Affirmation of the condensation of the inorganic layer's silicon dioxide tetrahedra is presented in the spectrum through the characteristic Si-O-Si stretching band near 1020 cm^{-1}. The immobilized *en* ligands from the organosilane precursor are also confirmed in the structure by multiple absorption bands found in the spectrum. The band at 1125 cm^{-1} corresponds to the wagging vibration of the Si-C bonds present in the material. The band of medium intensity near 1470 cm^{-1} is characteristic of the C-H scissoring vibration, and the sp^3-hybridized C-H stretching vibration is visible at 2920 cm^{-1}.[54,63]

Finally, the presence of secondary amines within the structure is shown in the spectrum may be located in the range of 1600 cm^{-1} to 1500 cm^{-1} in the IR spectrum, however it is difficult to see its common band in the mid-region of the spectrum due to significant overlapping. However, a weak peak is visible at 700 cm^{-1}, which is a characteristic of the typical wagging vibration exhibited by secondary amines. The N-H stretching band should also be covered by the broad -OH absorption band.[63] Coupling this information with the presence of hydrocarbon chains in the sample (along with EDS

results) is enough to suggest that the *en* ligands were successfully immobilized. It could also be suggested that the fairly intense absorption band at 1650 cm^{-1} represents the O-H bending vibration, rather than the typical C=O stretch in carbonyl compounds. This could arise from both the hydroxyl groups in the sample and interstitial water molecules trapped in the sample or KBr.

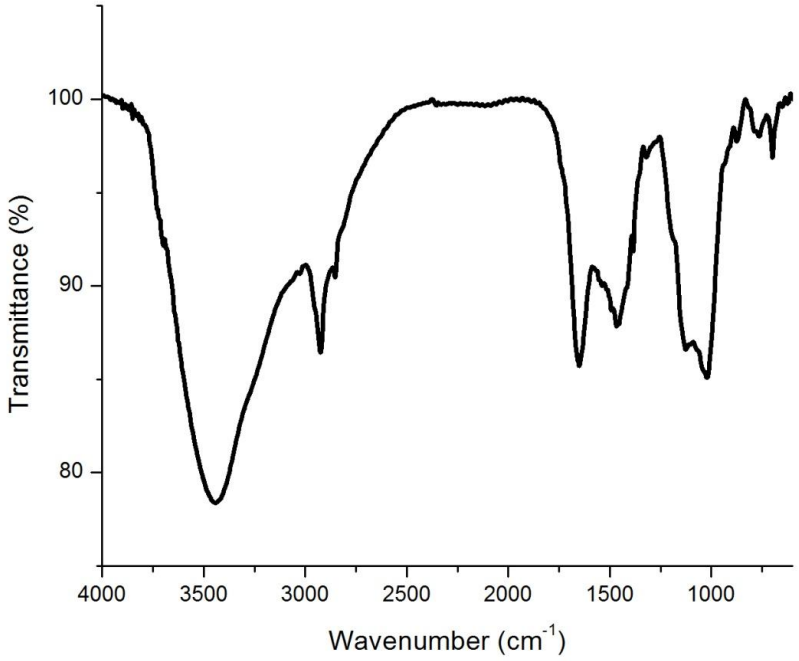

Figure 3.5 Infrared Spectrum of MgSi-b-*en*

3.1.4 Thermogravimetric Analysis

The TGA profile of MgSi-b-*en* (Figure 3.6) further confirmed the presence of organic groups incorporated into the organoclay material. As illustrated in the plot, the first drop in weight percentage occurs before 100 °C, which denotes the evaporation of trapped moisture in the structure. The next and only other weight decline that occurs

during analysis is observed by the large decrease in weight between 300 °C and 500 °C. This weight loss is associated with the decomposition of the organic groups (containing amine and carbon chains) in the parent material.

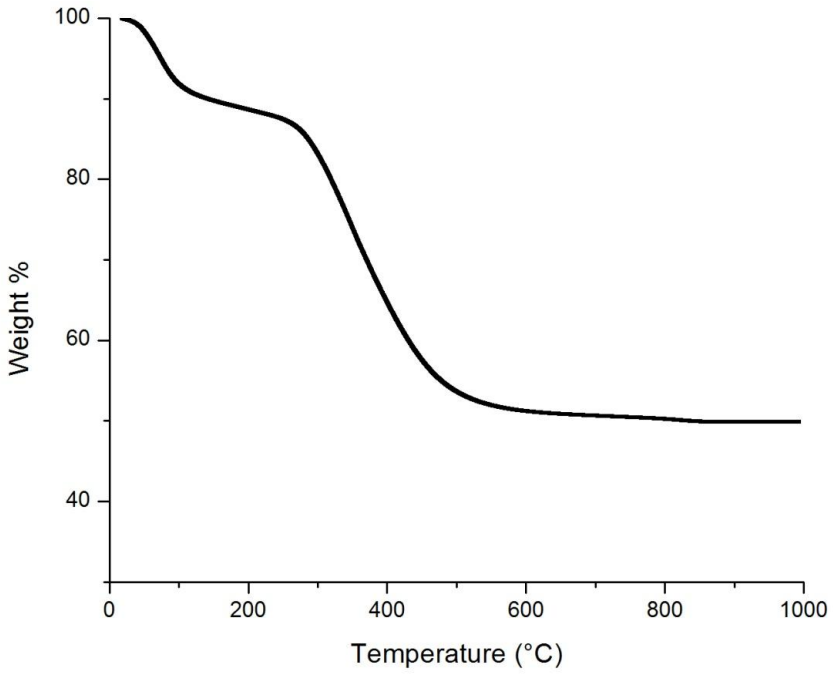

Figure 3.6 TGA Profile of MgSi-b-*en*

Quantification of the total organic groups is possible by measuring the difference in weight percentage that occurs during this large drop-off. After conversion and application of the mole ratio of *en* to total organic content, the estimated amount of ethylenediamine functionality in the material was calculated to be roughly 2.67 mmol/g. This number correlates to the theoretical adsorption capacity of MgSi-b-*en* as an adsorbent of heavy metal ions from aqueous solutions, assuming adsorption of the metal

cations operates via 1:1 monodentate complexation. This can be postulated because the chelating *en* groups may not be necessarily configured to allow polydenticity.

$$Weight\ Loss = 38\% \times 12.986\ mg$$

$$= 4.935\ mg \times \frac{1\ mmol\ total\ organic}{142.24\ mg} \times \frac{1\ mmol\ en}{1\ mmol\ total\ organic}$$

$$= 0.0347\ mmol \times \frac{1}{0.012986\ g} = 2.67\ mmol/g$$

3.2 Adsorption of Heavy Metal Ions with MgSi-b-*en*

3.2.1 Effect of pH

The effect of pH on the removal of metal ions from aqueous solutions proved to have significant influence on their adsorptive behavior. The initial concentrations of each metal ion were 100 ppm, while the dosage used the study was 0.2 mg/mL. The adsorption of each metal ion (Cu, Ni, Pb) achieved the highest capacity (Q_e) at a pH of 5 (Figure 3.7). At low pH, the prevalence of H^+ (protons) results in the protonation the amine groups, restricting the adsorption of metal cations, thus resulting in lower adsorption capacities. Above pH = 5, insoluble hydroxide species begin to form (though speciation varies among metals), and the adsorption capacities decrease towards zero. It was therefore determined that the optimal pH of adsorption for all metal systems was 5.

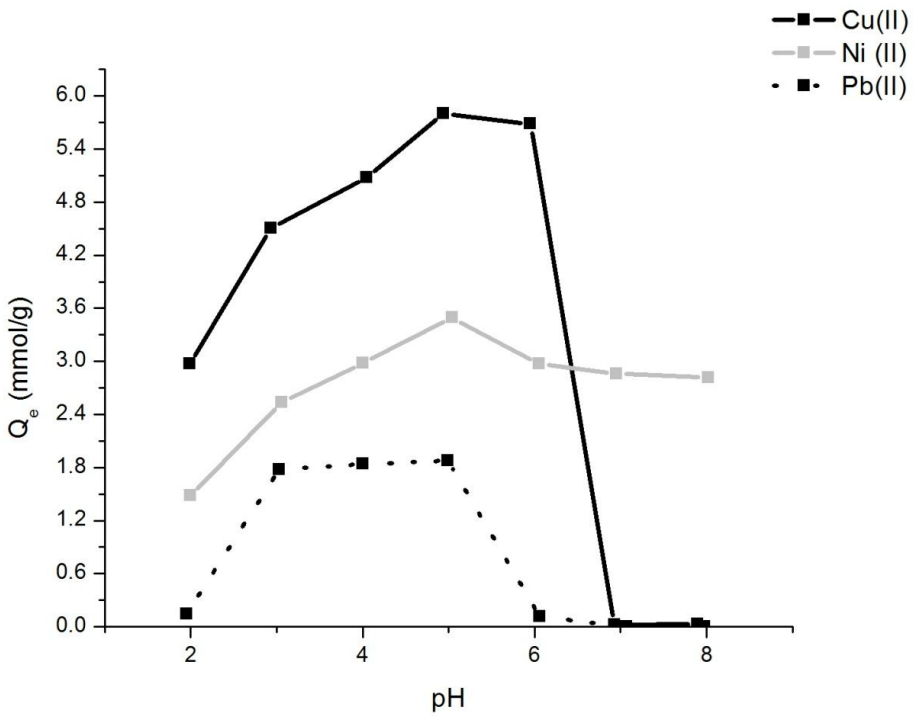

Figure 3.7 The effect of pH on adsorption of heavy metal ions with MgSi-b-*en*

3.2.2 Effect of Adsorbent Dosage

Further batch studies with MgSi-b-*en* were conducted to determine the effect of adsorbent dosage on the removal of heavy metal ions from solution (C_i = 100 ppm). Both the percentage removed and adsorption capacities for each metal was calculated based on dosage (Figure 3.8). For Cu(II) and Pb(II) systems, the percentage removal increases sharply until a saturation is reached around 0.25 mg/mL. The study reveals high uptake of copper and lead ions, resulting in almost 100% removal. This phenomenon is not visible for nickel adsorption, perhaps due to its smaller ionic radius or the affinity of *en* ligands towards Ni(II) ions. Analysing the effect of adsorbent dosage has revealed that using a dosage of 0.1 mg of adsorbent per mL of each metal ion solution resulted in the

highest Q_e values. Since percentage removal proved to vary amongst each metal, this dosage was selected as the optimal dosage to be used for the remainder of the adsorption studies.

(a)

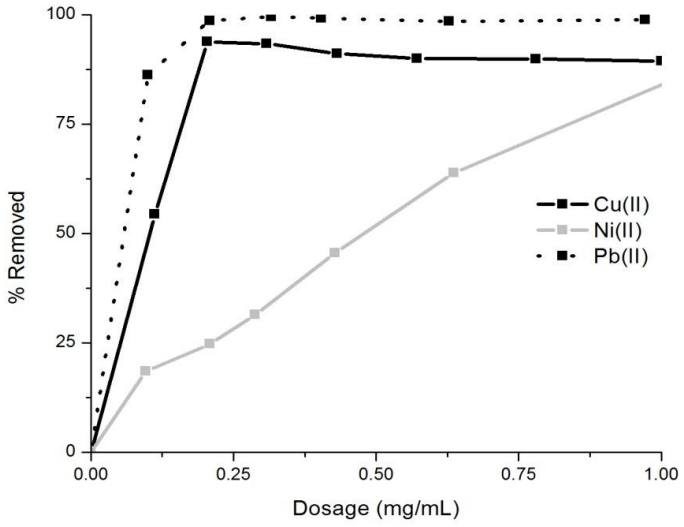

(b)

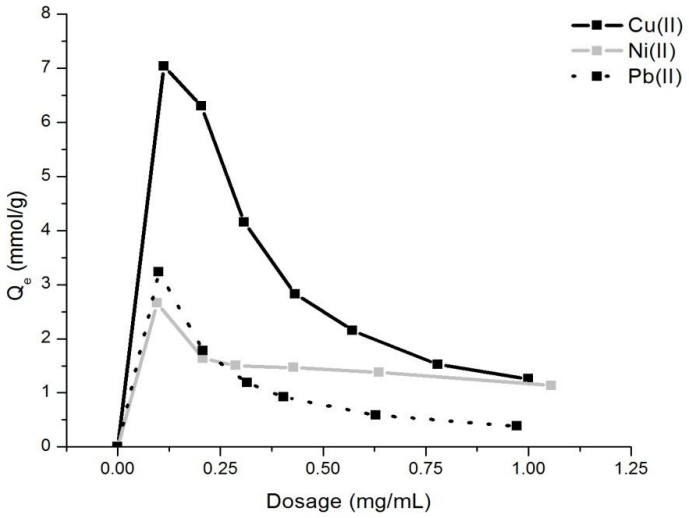

Figure 3.8 Effect of MgSi-b-*en* dosage on (a) percentage removed and (b) adsorption capacity of heavy metal ions

3.2.3 Effect of Contact Time

Examining the effect of contact time under the optimal dosage and pH conditions revealed that equilibrium was reached for adsorption of all metals after 5 hours of agitation time (Figure 3.9). For nickel adsorption, the saturation occurred at a Q_e of roughly 2.25 mmol/g, which closely resembles the calculated amount of *en* ligands in the material (~2.67 mmol/g - see *3.1.4 Thermogravimetric Analysis)*. Testing the effect of contact time on copper and lead adsorption, however, displayed higher loadings than the expected maximum. Conversely, the inset plot of Figure 3.9, which magnifies the lower contact times (up to 100 minutes), unveils a level of saturation followed by increasing adsorption capacities. The phenomenon is especially visible in Cu(II) adsorption, where uptake occurs very quickly and halts for a short period of time at a $Q_e \approx 1.35$ mmol/g before increasing nearly five-fold. The adsorption up to this plateau could be attributed to adsorption of copper ions by chemical forces - covalent bonding via *en* complexation. Further uptake and such high Cu(II) loadings could be attributed to adsorption through physical forces (i.e. van der Waals interactions). The trend is also visible for Pb(II) adsorption, however uptake past the expected capacity of MgSi-b-*en* is not as high as with Cu(II). This is mostly likely explained simply by the near-complete removal of the lead ions in solution by the adsorbent, given the high molar mass of lead. The capacity plateaus, though may be true, were calculated using a single batch experiment, and therefore would need to be confirmed. However, it is still reasonable to suggest further adsorption via physisorption simply due to the higher uptake than the expected adsorption capacity.

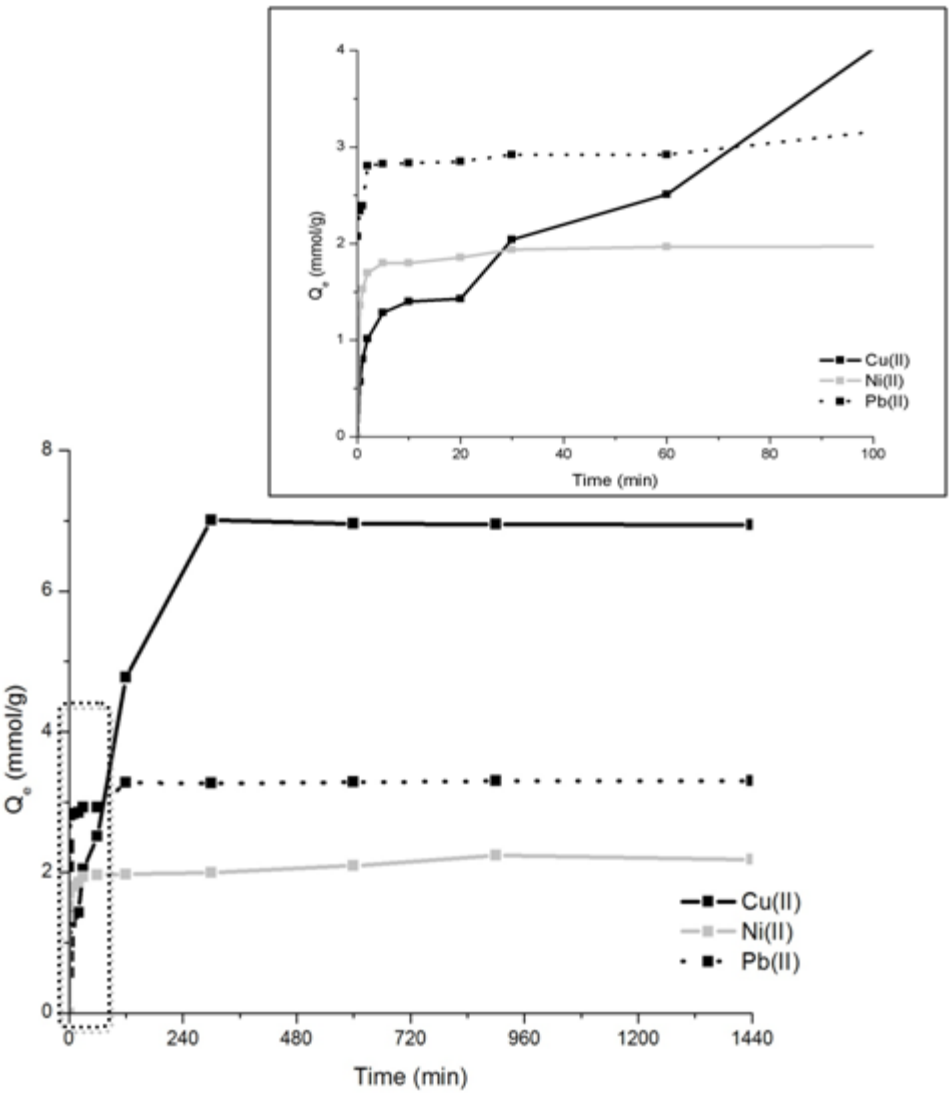

Figure 3.9 Effect of contact time on heavy metal adsorption with MgSi-b-*en*

Applying the pseudo-second order model to the data gives linear relationship for all metal ions (Figure 3.10). As outlined in the experimental section, the PSOE operates by the assumption that chemical adsorption through the active *en* sites and the metal ions on the surface of the material is the rate-limiting step. Though this adsorption process initially operates by chemisorption, it was shown previously that the active sites become saturated and uptake of metal ions proceeds past the expected adsorption capacity. It can

be seen on the inset graph that the model is more applicable at lower uptake periods, given the higher correlation coefficients. This relates to the assumptions of the PSOE, along with the current understanding of MgSi-b-*en*. Initial adsorption occurs through chemical forces, but as contact time increases, the applicability of the model diminishes, as physical interactions are allowed. A more appropriate rate-limiting step, such as a diffusion mechanism, can then be suggested to describe the kinetics of adsorption.

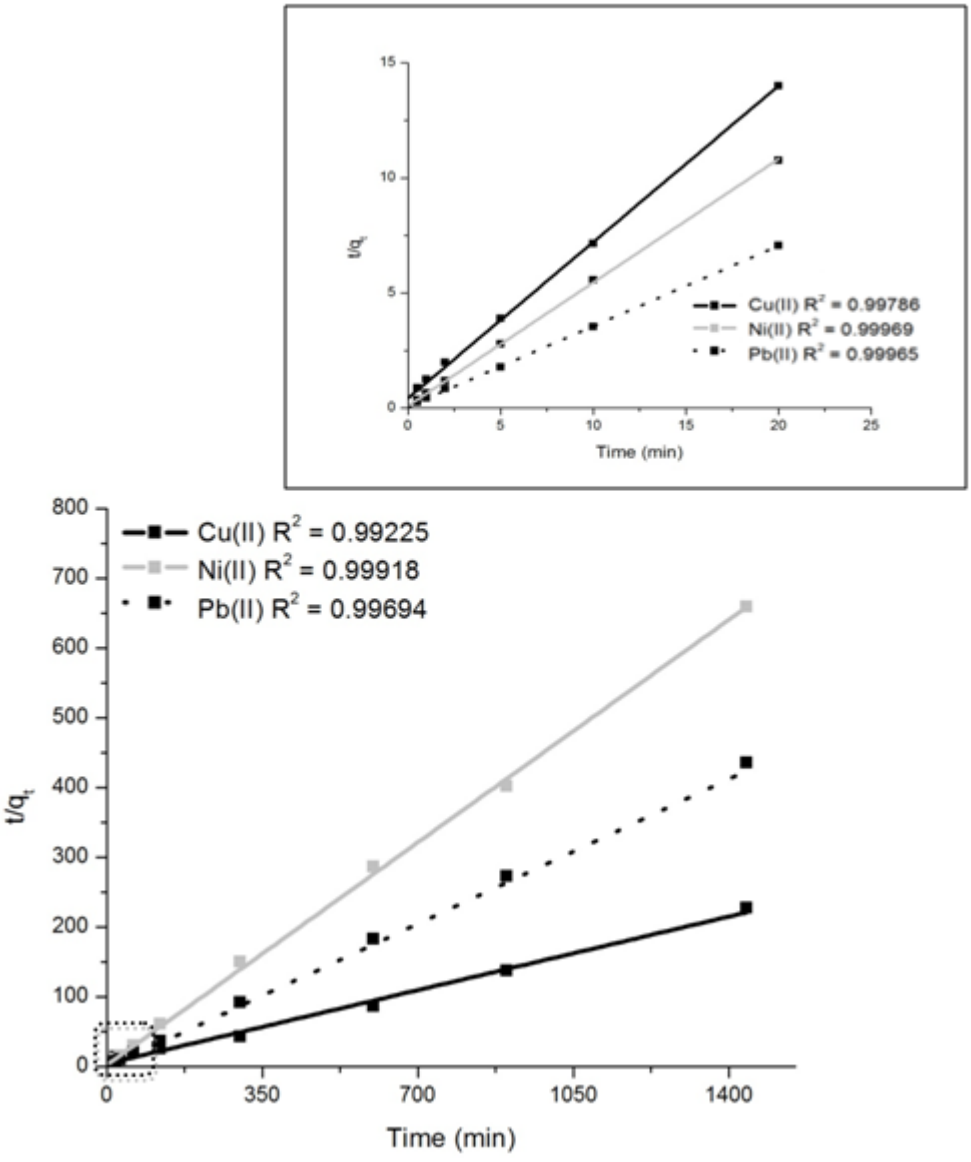

Figure 3.10 MgSi-b-*en* kinetics of adsorption - pseudo-second order model

3.2.4 Adsorption Isotherms

Adsorption isotherms for all of the metal ion systems were constructed and the results are shown in Figure 3.11. The plots clearly indicate high adsorption capacities for all metal ions, under optimal pH levels, dosages, and agitation times. As illustrated by the isotherms, high uptake occurs at low equilibrium concentrations, but rather than saturating at higher concentrations, a gradual increase in adsorption capacity is prevalent. The trend is more apparent in copper and lead systems than in nickel. Similar to contact time studies, the adsorption of Cu(II) and Pb(II) ions reach higher Q_e values than the expected maximum determined by TGA. Such high adsorption capacities at high equilibrium concentrations are further indications of adsorption by physical forces after saturation of active sites on the material's surface.

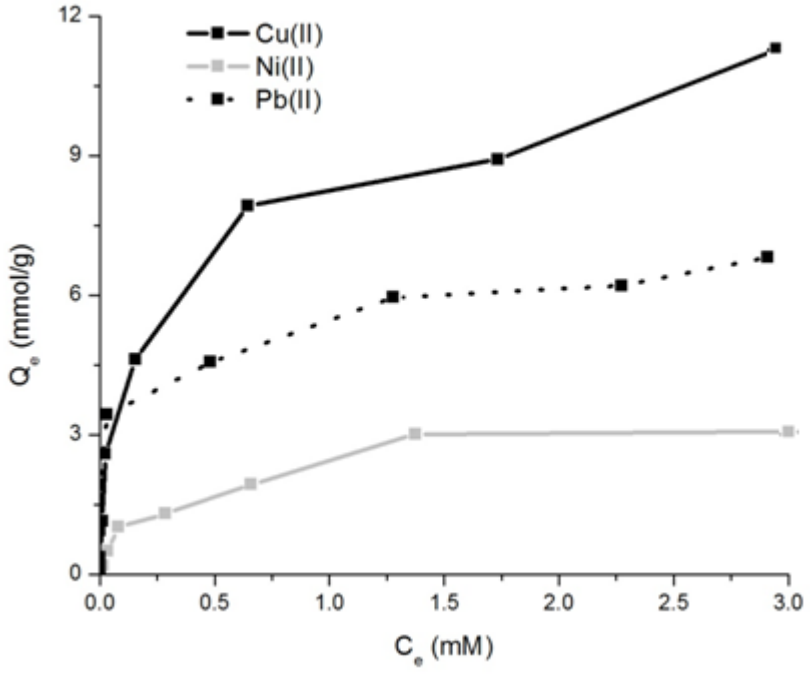

Figure 3.11 Adsorption isotherms for all metals with MgSi-b-*en*

The adsorption isotherm results illustrate a deviation from the typical Langmuir isotherm model. For each of the metal systems the rapid and high uptake at low equilibrium concentrations can often be described by the Langmuir adsorption isotherm. However, the characteristic plateau of Langmuir-type adsorption is nonexistent in each of the adsorption isotherms, especially in Cu(II) and Pb(II) systems. The continuous uptake of metal ions past the saturation of the active sites supports the concept of nonspecific adsorption onto the material surface, which is often described by the Freundlich isotherm model. The profiles for each metal system in this study exhibit this Freundlich behavior at high equilibrium concentrations, further indicating the adsorption of metal ions after saturation of the *en* surface sites via physical interactions (i.e. van der Waals).

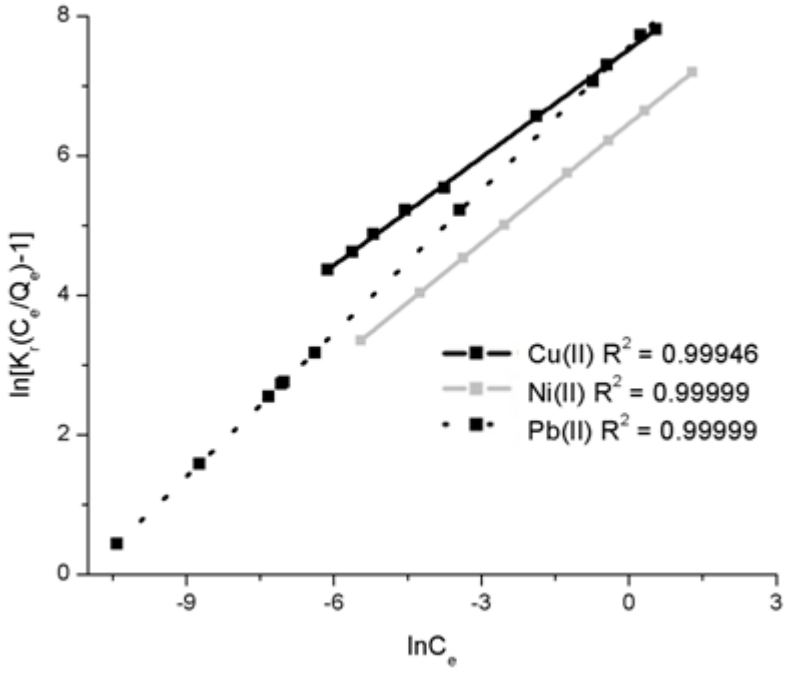

Figure 3.12 Redlich-Peterson isotherm models for MgSi-b-*en*

The adsorption of copper, nickel, and lead ions onto MgSi-b-*en* can ultimately be described by the Langmuir model at low metal concentrations and by the Freundlich model at higher concentrations. This behavior has been previously noticed, and a new three-parameter isotherm has been constructed to describe it - the Redlich-Peterson isotherm model.[60-61]

$$q_e = \frac{K_r C_e}{1 + a_r C_e^{\beta}} \quad (6)$$

Where K_r and a_r are Redlich-Peterson constants, having units of (L/mol) and $(L/mol)^{\beta}$, respectively, and the exponent β relates to the equilibrium concentration. The exponent tends towards one at low concentrations when Langmuir conditions dominate the system. At high concentrations with Freundlich behavior, β decreases towards zero. Because it is a three-parameter equation, graphing $\ln[K_r(C_e/Q_e) - 1]$ vs $\ln(C_e)$ requires a minimization procedure to maximize the correlation coefficient R^2 of linear plot.[60-61] Figure 3.12 shows the isotherms of copper, nickel, and lead adsorption fitted to the Redlich-Peterson model, and Table 3.1 compares the correlation coefficients of the Langmuir, Freundlich, and Redlich-Peterson models for each system.

	Langmuir	**Freundlich**	**Redlich-Peterson**
Copper	0.9154	0.8545	0.9995
Nickel	0.9832	0.9390	0.9999
Lead	0.9477	0.7892	0.9999

Table 3.1 Correlation coefficients of adsorption isotherms for the adsorption of Cu(II), Ni(II), and Pb(II) with MgSi-b-*en*

3.2.5 Multi-Component Adsorption

For each binary metal system, the effect of saturation was examined by varying metal ion concentrations based on the theoretical adsorption capacity, 2.67 mmol/g. Multiple combinations of under-capacity, at-capacity, and over-capacity concentrations were prepared for adsorption studies. For example, in a binary copper-nickel system, the adsorption of Cu(II) ions was analysed at various levels of capacity (under-capacity copper - UCC, at-capacity copper - ACC, over-capacity copper - OCC). Assigned as the primary ion, each concentration of copper was then measured against different concentrations of nickel (also based on capacity). As the secondary ion, each solution contained its designated under-capacity (UCN), at-capacity (ACN), and over-capacity (OCN) nickel content.

Specific adsorption of each metal ion in binary systems followed the expected behaviour, based on formation constants of metal-*en* complexes. In all systems analysed, adsorption capacities (Q_e) and selectivity coefficients (*k*) were calculated for each metal ion. The selectivity coefficient is based on the relationship between the partition coefficients (K_d) of each ion in the system, for example:

$$k_{Cu} = \frac{K_d\,(Cu)}{K_d\,(Ni)} \qquad K_d = \frac{A_e}{C_e}\ \text{(L/g)} \qquad (7)$$

Where A_e is the moles of adsorbed species per gram of adsorbent at equilibrium (mmol/g) and C_e is the equilibrium concentration in solution (mM). The units on K_d allow *k* values to be reported as unitless quantities. Higher specificity towards a given species in a multi-component solution results in $k \geq 1$.

In solutions containing both copper and nickel ions (Figure 3.13), higher specificity towards copper ions was regular throughout the assay. Increasing Cu(II)

concentration in the system caused both an increase in Q_e and *k*. Increasing the Ni(II) concentrations had little effect on the Q_e of copper adsorption, but it did alter *k*. Regardless of the level of capacity of copper in the binary system, increasing the Ni(II) concentrations reduced the selectivity of MgSi-b-*en* towards Cu(II) over Ni(II). However, the values of *k* are still high at large concentrations of nickel.

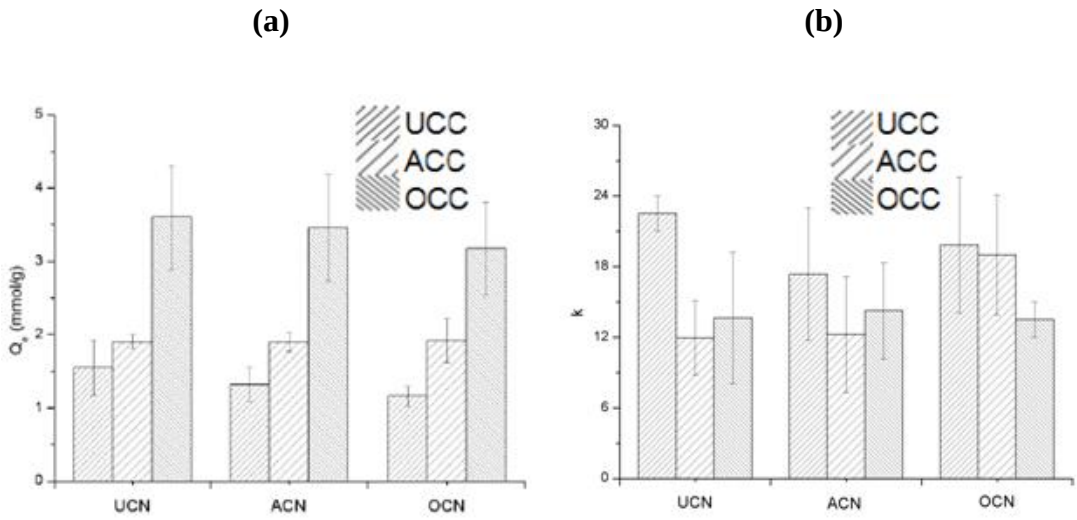

Figure 3.13 (a) Adsorption capacities and (b) selectivity coefficients of Cu(II) adsorption in binary Cu/Ni Systems

The reverse effect can be seen in Figure 3.14, which illustrates the Q_e and *k* of nickel adsorption in binary Cu(II)/Ni(II) systems. The adsorption capacity of nickel is influenced more by the concentration of copper in the system than the capacity for copper, but the effect is still minimal. All systems exhibited $Q_e > 1$, which was expected due to the lower affinity of *en* ligands towards Ni(II) ions. The effect of concentration of the secondary ion (Cu) once again proved to have more of an effect on the value of *k* than the Q_e. Increasing copper concentrations to at-capacity levels inhibited the adsorption of

nickel ions onto the material. The selectivity coefficients were very small for Ni(II) adsorption (k<1) compared to that for Cu(II) adsorption.

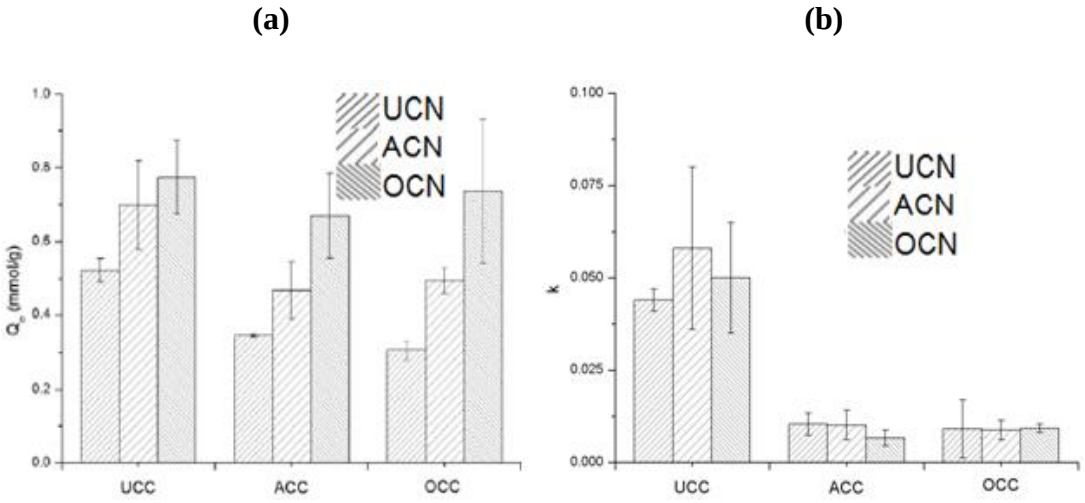

Figure 3.14 (a) Adsorption capacities and (b) selectivity coefficients of Ni(II) adsorption in binary Cu/Ni Systems

The binary solutions of copper and lead (with varying degree of capacity) were also studied in specificity assays (Figure 3.15). Capacities for copper ions were lower than the previous ones in the Cu(II)/Ni(II) systems, indicating a higher specificity towards lead ions. Increasing lead concentration had more of an effect on the adsorption capacity for copper, most likely due to blockage of active sites by the larger Pb(II) ion. Surprisingly, a reverse trend was observed in the selectivity coefficients for Cu(II) in the binary system. Increasing lead concentration in fact resulted in higher k for copper adsorption. This could also be related to ionic radius, in which higher amounts of lead may block access to surface functional groups to same large Pb(II) ions, but smaller Cu(II) ions may be permitted to be adsorbed into the pores. Conversely, higher capacities for lead ions in the binary Pb(II)/Cu(II) systems are observed (Figure 3.16), and increasing the concentration of copper in solution does not alter the Q_e for lead

adsorption. In terms of the selectivity coefficients, increasing the secondary ion (Cu) concentration once again decreases the specificity of the adsorbent towards the primary lead ions. However, *k* values of Pb(II) for all of the under-capacity, at-capacity, and over-capacity solutions are over 20 times higher than *k* for Cu(II).

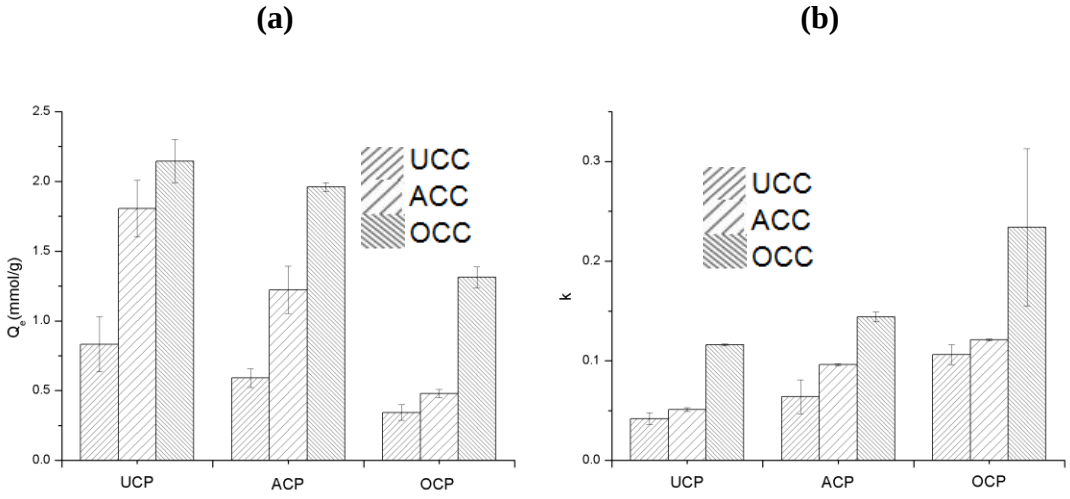

Figure 3.15 (a) Adsorption capacities and (b) selectivity coefficients of Cu(II) adsorption in binary Cu/Pb Systems

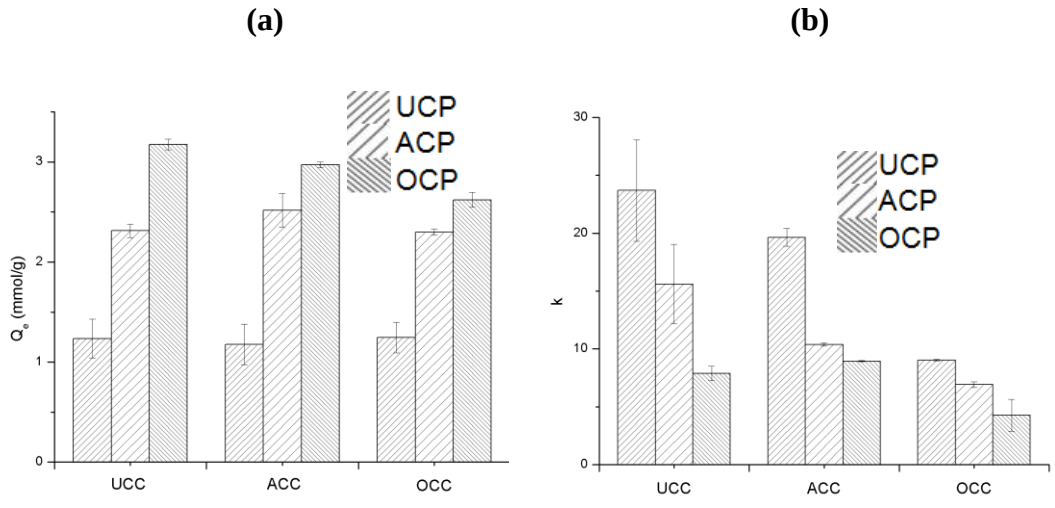

Figure 3.16 (a) Adsorption capacities and (b) selectivity coefficients of Pb(II) adsorption in binary Cu/Pb Systems

Finalizing the binary adsorption studies (Figure 3.17), nickel and lead systems were analysed to reveal an even higher specificity of MgSi-b-*en* towards lead ions. The adsorbent exhibited the lowest adsorption capacities for Ni(II) out of all multi-component systems, along with the smallest *k* values. The effect of concentration of the secondary ion (Pb) on Q_e was perhaps the largest out of all of the studies as well, with decreasing capacities with increasing lead content. Although the selectivity coefficients were altered due to saturation of the adsorbent with lead ions, the values were very small, indicating almost no specificity towards Ni(II) in nickel-lead systems. The *k* of nickel ions also exhibited the same increasing trend as the copper ions versus the rising degree of capacity of lead in solution. Again, this could be attributed to the larger ionic radius of the lead ions.

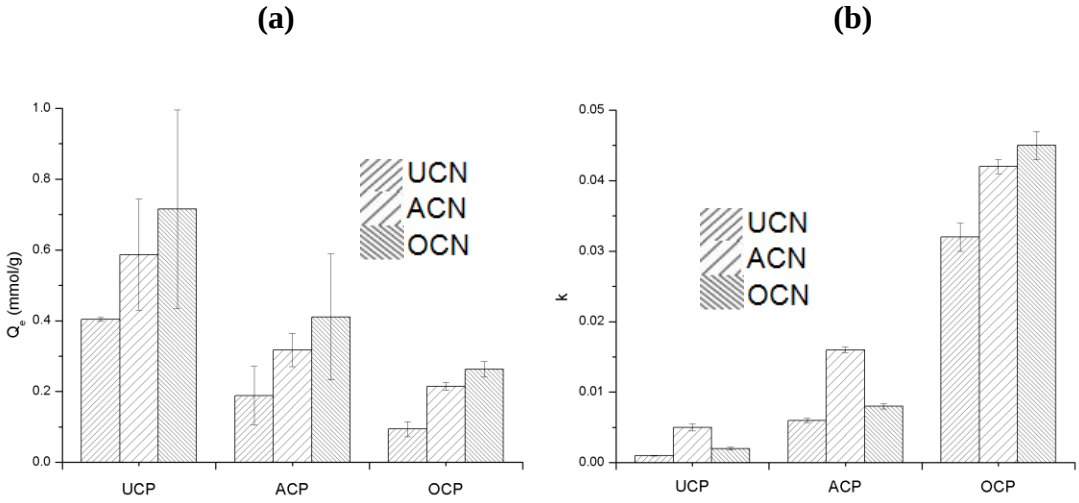

Figure 3.17 (a) Adsorption capacities and (b) selectivity coefficients of Ni(II) adsorption in binary Ni/Pb Systems

Adsorption capacities and selectivity coefficients for lead (Figure 3.18) were comparable to those in the Cu(II)/Pb(II) binary systems, with the concentration increase of the secondary ion nickel having relatively no effect on the Q_e. However, both the

Ni(II) and Pb(II) concentrations did have an effect on the *k* for lead. Under-capacity solutions of lead showed extremely high *k* values, which decreased as saturation was achieved. This is simply due to lower amounts of metal ions in solution that result in the nearly complete removal of lead, resulting in a high *k*. Moreover, altering the concentration of nickel ions in the system only had an effect on these under-capacity lead solutions.

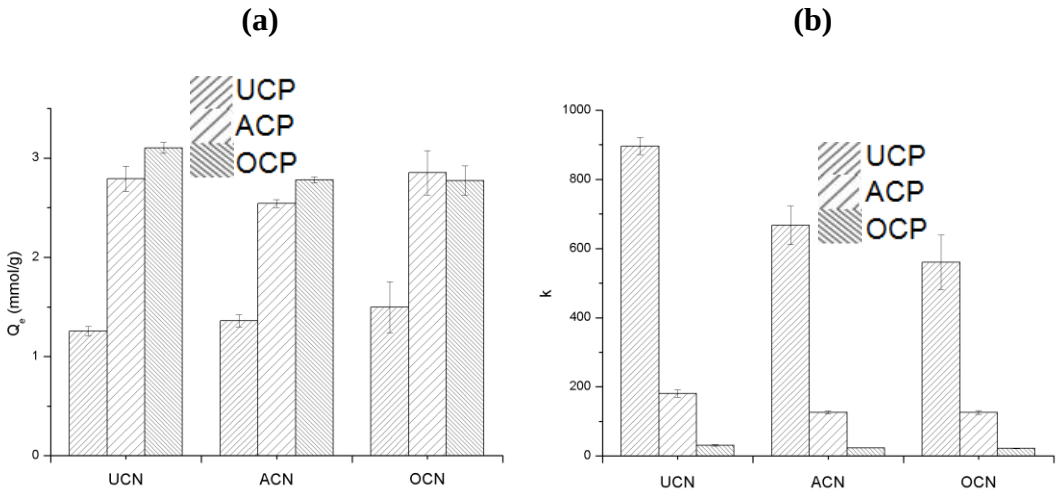

Figure 3.18 (a) Adsorption capacities and (b) selectivity coefficients of Pb(II) adsorption in binary Ni/Pb Systems

3.3 Synthesis and Characterization of Imprinted Adsorbent

3.3.1 Synthesis of Ion-Imprinted Organoclays

Due to the limited solubility of lead nitrate in alcohols, the ion-imprinting procedure could not be performed using lead ions. Though a product was able to be produced by combining all precursors in a single beaker containing $Pb(NO_3)_2$, Pb-*en* complexation was not confirmed. Moreover, basic hydrolysis would cause the precipitation of lead hydroxide species. Therefore, MgSi-b-*en*±Pb was eliminated from this study.

After washing the imprinted organoclays with 5M HCl, the materials went from the colour of the metal-*en* complex to a yellow colour similar to that of the parent compound, MgSi-b-*en*. As mentioned in the experimental section, the metal ion concentrations of the stripped adsorbents were compared to the loaded ones to determine the efficacy of the stripping method (Table 3.2). Washing the materials with such a strong (mineral) acid causes damage to the entire clay structure. Though the acid will strip the imprinted metal ions within the material, it will also dissolve its magnesium backbone. By performing the stripping procedure in the ethylenediamine solution under reflux, the structural integrity of the material was maintained.

	mmol Cu(II)/g adsorbent	**mmol Ni(II)/g adsorbent**	**% Removed**
MgSi-b-*en*(+Cu)	**4.79**	**N/A**	**--**
MgSi-b-*en*(-Cu)	**0.59**	**N/A**	**87.7%**
MgSi-b-*en*(+Ni)	**N/A**	**1.32**	**--**
MgSi-b-*en*(-Ni)	**N/A**	**0.65**	**51%**

Table 3.2 Stripping efficacy on ion-imprinted adsorbents with ethylenediamine solution

The results in Table 3.2 indicated that each metal ion (copper and nickel) caused the imprinting procedures to vary. The total copper content in MgSi-b-*en*(+Cu) was significantly higher than the expected adsorption capacity determined by TGA. Though

this appears to be counterintuitive, excess copper ions (that did not form complexes with the organosilane prior to synthesis) could have physically adsorbed to the clay surface. Conversely, nickel ions only formed complexes with *en* ligands that were present in the synthesis of MgSi-b-*en*(+Ni). These assumptions are reasonable because the adsorbent has already proven to be an effective adsorbent for large amounts of Cu(II) ions, indicated by the copper adsorption isotherm. Furthermore, the higher affinity of the *en* ligands towards Cu(II) over Ni(II) is evident when comparing the metal contents of each loaded adsorbent. The removal efficacy of the ethylenediamine solution is considerably higher in the copper ion-imprinted material, again indicating preference towards Cu(II) ions.

3.3.2 Characterization of Loaded and Stripped Organoclays

Upon implantation of the metal ions (Cu, Ni) into the organoclays via the ion-imprinting procedure outlined in the experimental section, the products obtained exhibited the same colour as the *en* complexes formed in solution prior to condensation. XRD patterns of both of the copper(II) ion-imprinted adsorbents (Figure 3.19) and the nickel(II) ion-imprinted materials (Fig 3.20) were obtained. Though less defined than those of the parent compound, the typical peaks exhibited by talc-like materials can be seen in each spectrum. Again, the peak associated with the 001 reflection plane of talc is not visible in any of the patterns, suggesting a non-lamellar arrangement. The other reflection plane peaks associated with talc mineral, and as seen in the XRD pattern of MgSi-b-*en*, are all visible in the spectra. MgSi-b-*en*(+Cu) exhibited the lowest degree of crystallinity, illustrated by broader and less defined diffraction peaks. However, the

disorder may be attributed to the large amount of Cu(II) ions adsorbed onto the material surface, as indicated by the acid leaching test.

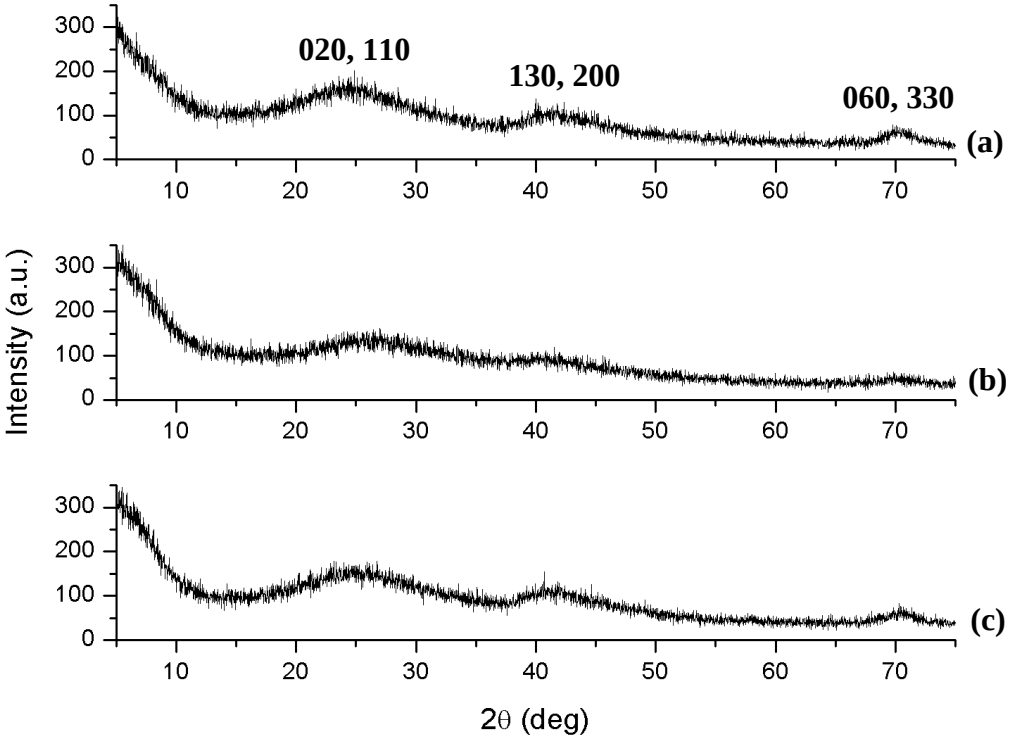

Figure 3.19 XRD patterns of a) parent adsorbent MgSi-b-*en*, (b) copper ion loaded MgSi-b-*en*(+Cu), and (c) stripped copper ion MgSi-b-*en*(-Cu)

Some of the typical talc peaks are once again observed upon removal of the copper ions. The loaded material exhibits less intense diffraction peaks, suggesting that the copper ions may block the diffraction of X-rays off of the reflection planes of the material. Several interesting peaks are observed in both the loaded and stripped nickel ion-imprinted materials, especially at $2\theta \approx 45°$. Each of these peaks decrease in intensity as the nickel ions are stripped from the material, since roughly 50% of the Ni(II) ions were removed by the ethylenediamine solution. It is reasonable to suggest that these

peaks are characteristic of formed nickel nanoparticles.[64-65] Moreover, it differs from the Cu(II) ion-imprinted adsorbents in that there is a significantly smaller amount of ions in the material, which may have an effect on the overall structure. These peaks exhibited in the XRD pattern of the Ni(II) ion-imprinted materials could possibly result from the formation of Ni nanoparticles that become trapped in the porous clay material.

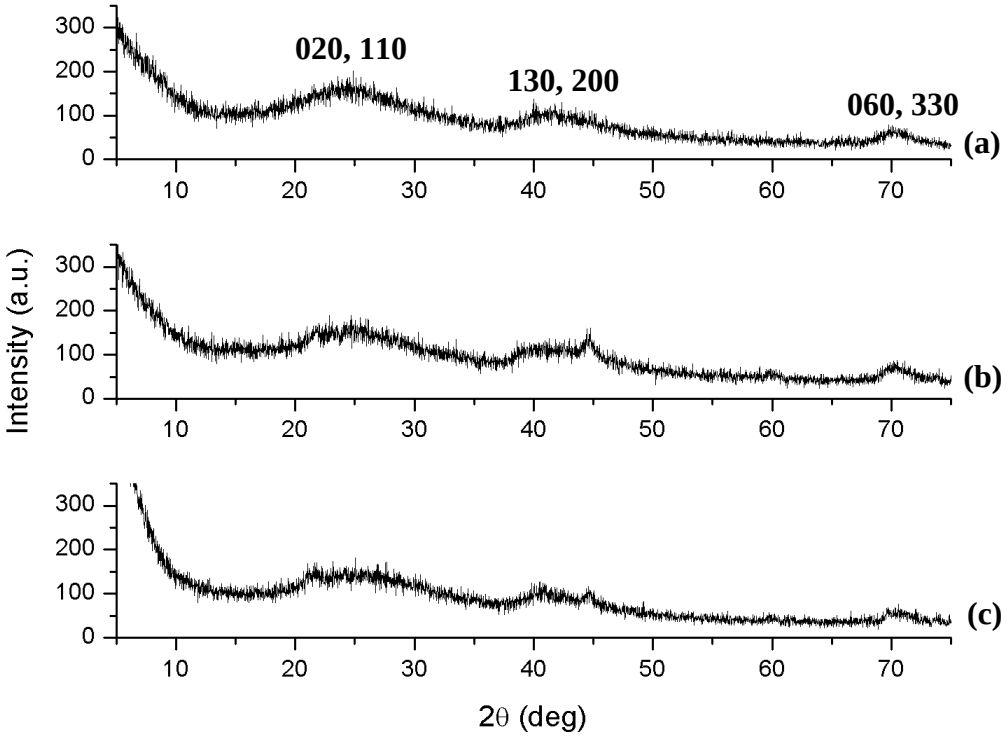

Figure 3.20 XRD patterns of (a) parent adsorbent MgSi-b-*en*, (b) nickel ion loaded MgSi-b-*en*(+Ni), and (c) stripped nickel ion MgSi-b-*en*(-Ni)

The N_2 adsorption isotherms of the loaded and stripped copper(II) ion-imprinted clays (Figure 3.21) gave noticeably different profiles than the parent material, MgSi-b-*en*. The calculated BET surface areas of both the loaded adsorbents and the stripped, imprinted materials are given in Table 3.3. The isotherm of MgSi-b-*en*(+Cu) varies

significantly from the parent material, clearly exhibiting a higher degree of multilayer adsorption. The isotherm gives less of an indication of mesopores, but rather the presence of large voids in the structure, in addition to micropores, typical of organoclays.[35-41] The isotherm illustrates type II behaviour like the parent's isotherm. The presence of a large amount of copper ions on the material surface leads to the assumption that the ions essentially eliminate the mesoporosity in the hybrid clay. The profile of MgSi-b-*en*(-Cu) was completely altered from its ion-loaded counterpart. The isotherm also displayed type I behaviour,[62] which resembles the Langmuir isotherm. It is clear that the gas adsorption is initially strong, but the adsorption plateaus after the micropores of the solid are filled, and there may be no large pores for multilayer adsorption to occur. This also indicates a lack of external surface area, which agrees with the large decrease in the calculated BET surface area (Table 3.3).

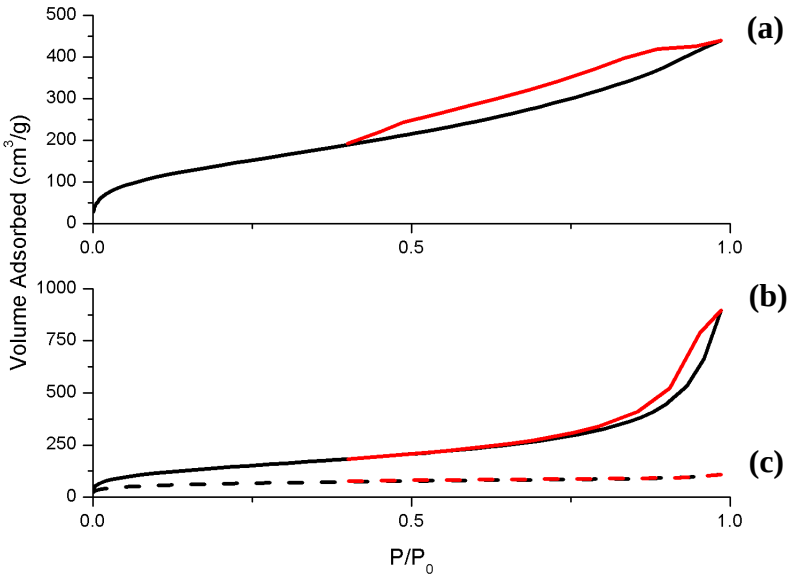

Figure 3.21 N_2 adsorption isotherms of (a) parent adsorbent MgSi-b-*en*, (b) copper ion loaded MgSi-b-*en*(+Cu), and (c) stripped copper ion MgSi-b-*en*(-Cu)

The loaded and stripped nickel(II) ion-imprinted adsorbents displayed isotherms that were very similar to each other (Figure 3.22). The isotherm of MgSi-b-*en*(-Ni) was a near replicate of the nickel-loaded material, which is in agreement with the results of the stripping procedure that previously revealed it was not as effective for nickel desorption as copper. The profile of MgSi-b-*en*(+Ni) once again exhibits a type II isotherm, but a lower amount of gas molecules are adsorbed onto the multilayer. In fact, the isotherm is more similar to the parent adsorbent's isotherm, but it resembles the less-porous nature of the copper-loaded adsorbent. Since the adsorbent is not saturated with nickel ions, the formation of nickel nanoparticles (as evidenced by XRD analysis) may cause pore blockage as well. The calculated BET surface areas of MgSi-b-*en*(+Ni) and MgSi-b-*en*(-Ni) also showed no significant difference (Table 3.3).

	Surface Area (m^2/g)	**Isotherm Type**
MgSi-b-*en*(+Cu)	**523.95**	**II**
MgSi-b-*en*(-Cu)	**230.56**	**I**
MgSi-b-*en*(+Ni)	**465.07**	**II**
MgSi-b-*en*(-Ni)	**459.26**	**II**

3.3 BET surface areas of ion-imprinted ethyelenediamine-functionalized organoclays

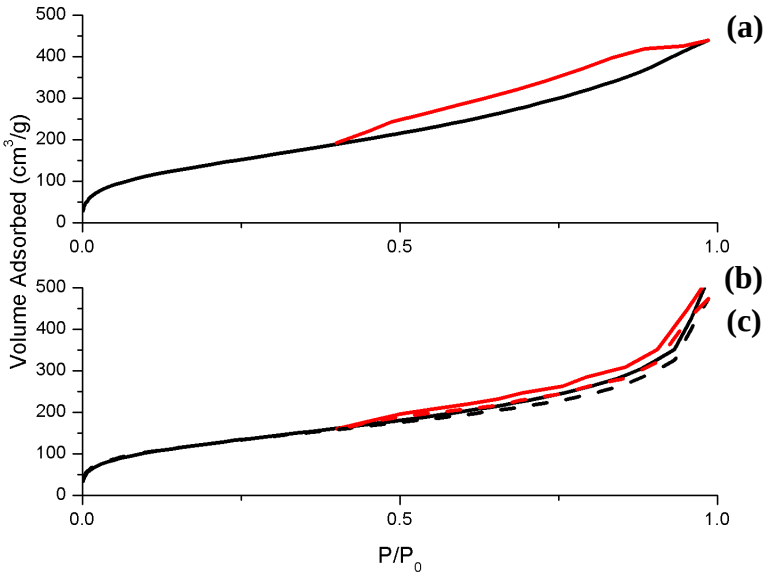

Figure 3.22 N_2 adsorption isotherms of (a) parent adsorbent MgSi-b-*en*, (b) nickel ion loaded MgSi-b-*en*(+Ni), and (c) stripped nickel ion MgSi-b-*en*(-Ni)

The SEM images of the Cu(II) ion-imprinted adsorbents (Figure 3.23) showed that magnesium phyllosilicate sheets were again formed in the synthesis procedure. Like the parent material, the plates were disordered rather than lamellar. At roughly 20 μm, the diameter of the sheets were essentially 1/5th that of the parent's. In addition, the particles of the Cu(II) loaded material (a and b) were more closely packed, but at the same time the surfaces were more exposed, which may explain the high volume of gas molecules adsorbed onto the multilayer in the N_2 adsorption isotherm. Rather than overlapping and stacking, the sheets appeared to assemble on a flat plane, exhibiting a network of pore-like crevices. The EDS results also indicated the presence of copper on the surface of the phyllosilicate sheets. Upon leaching of the copper ions from the material, the particles became even closer packed, and the sheets exhibited a "stacked" morphology (c and d). However, this stacking was not lamellar, as proven by the XRD

pattern, but more of a disordered overlap, coupled with the elimination of the pore-like channels. This would explain the lower surface area and change in the N_2 isotherm shape. The typical peak for copper was also eliminated in the EDS spectrum of MgSi-b-*en*(-Cu), indicating that the stripping procedure was successful.

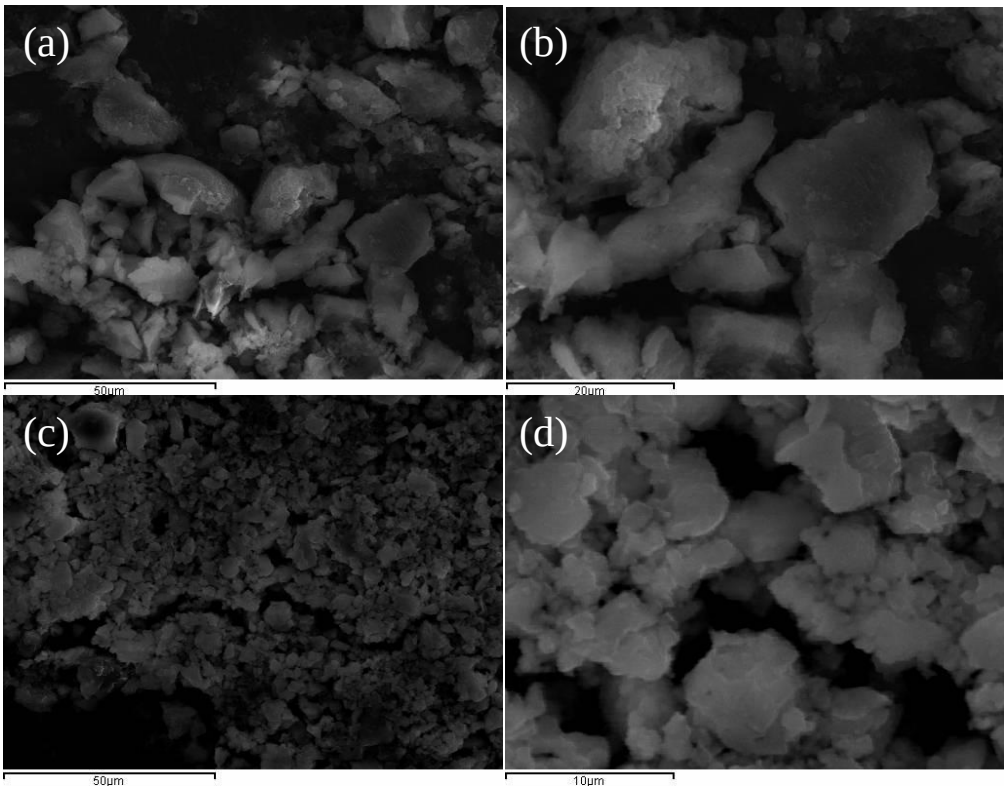

Figure 3.23 SEM images of (a,b) copper ion loaded MgSi-b-*en*(+Cu) and (c,d) stripped copper ion MgSi-b-*en*(-Cu)

The SEM images of the Ni(II) ion loaded adsorbent (Figure 3.24, a and b) gave a similar morphology to the Cu(II) ion loaded material. The particles, however, drastically varied in size and shape. Some of the particles did not exhibit the typical phyllosilicate sheet morphology. and it is plausible that these structures are nickel nanoparticles. Since the complexation between the nickel ion and the organosilane was not as strong as copper, the EDS spectrum indicated that nickel on the surface of the material was not

homogeneously distributed across all of the material. The morphology of the stripped nickel ion adsorbent, MgSi-b-*en*(-Ni) (c and d), was similar to MgSi-b-*en*(-Cu) at lower magnification. Increasing the magnification reveals aggregated particles (d), which may be caused by the ethanol, or remaining nickel nanoparticles. The decreased efficacy of the ethylenediamine stripping method is evident in the magnified image (d) of the stripped adsorbent, as the general morphology of the sheets does not differ significantly from the nickel ion loaded structure. Though the EDS results indicate a lower Ni content on the surface of the material, it is still present.

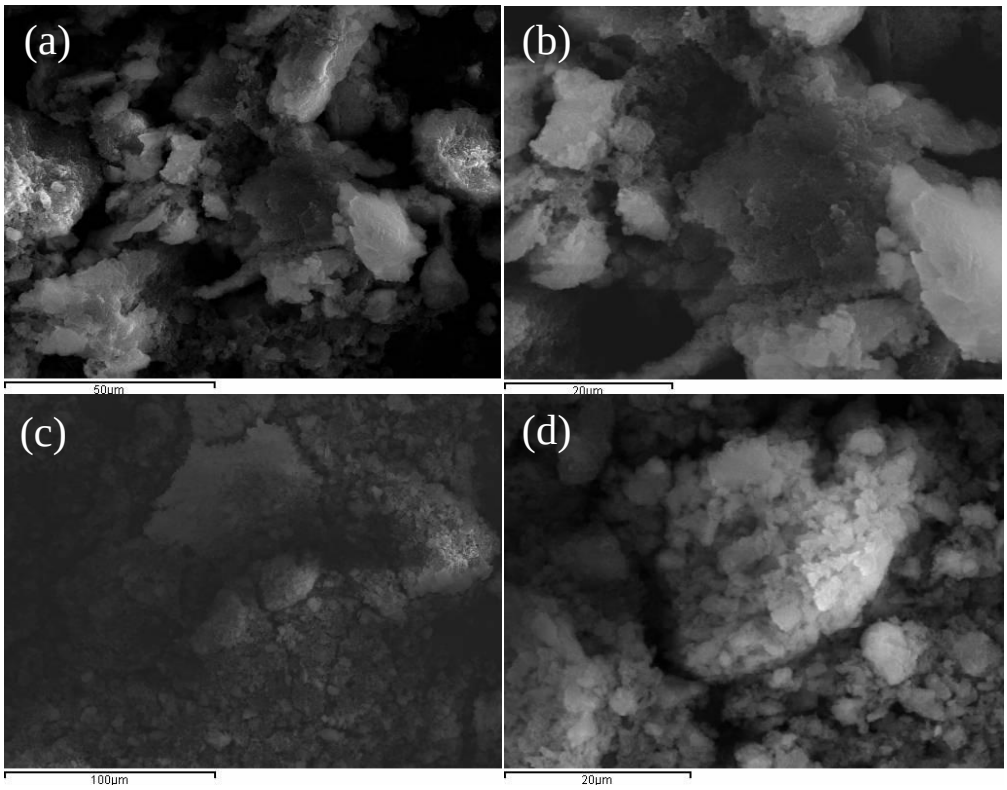

Figure 3.24 SEM images of (a,b) nickel ion loaded MgSi-b-*en*(+Ni) and (c,d) stripped nickel ion MgSi-b-*en*(-Ni)

The IR spectra of the copper-imprinted organoclay adsorbents are compared to the parent (a) adsorbent in Figure 3.25. It is clear that the Cu(II)-loaded clays possess the

same functional groups as the parent material. The most obvious difference in the ion-loaded organoclay (b) is the immergence of a strong, sharp band at 1380 cm^{-1}, which seems to overlap the C-H bending vibration band at 1470 cm^{-1}. Though the material was washed after synthesis, this band gives evidence of the presence of NO_3^- anions arising from the metal salts.[66] After removing the metal ions, the IR spectra of the absorbent (c) once again resembles the parent spectrum due to the disappearance of this strong band. Nearly the exact same spectra as the copper-imprinted organoclays are observed for the nickel-imprinted materials (Figure 3.26). Differences in intensity of the absorption bands arise simply due to the variance in amount of material contained in the KBr pellet.

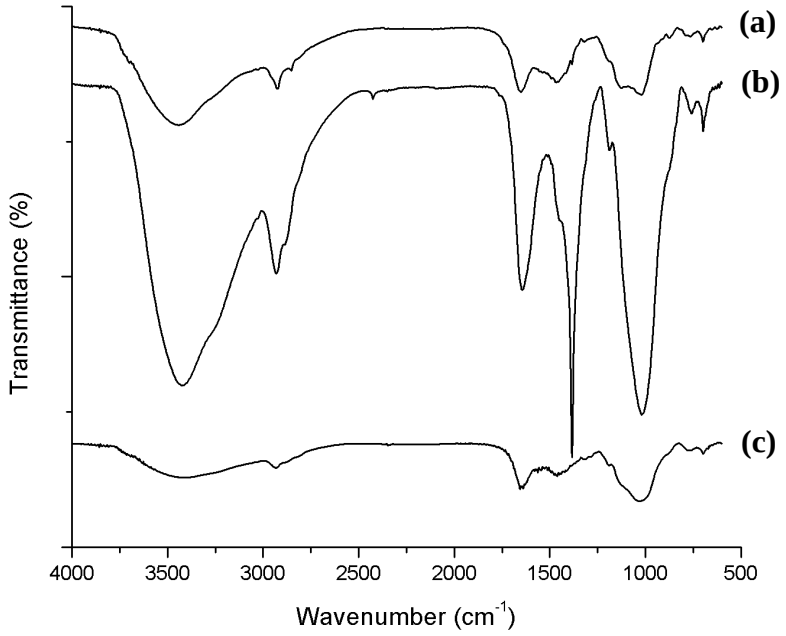

Figure 3.25 IR spectra of (a) parent adsorbent MgSi-b-*en*, (b) copper ion loaded MgSi-b-*en*(+Cu), and (c) stripped copper ion MgSi-b-*en*(-Cu)

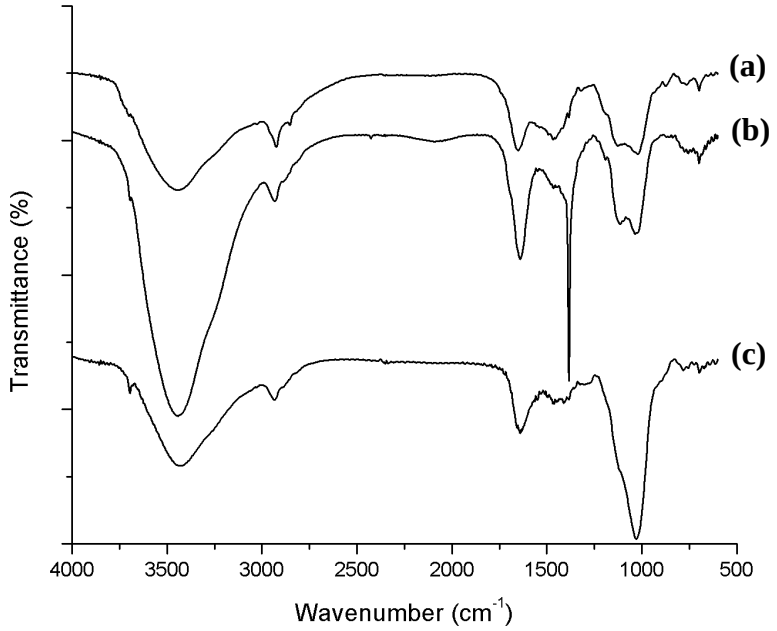

Figure 3.26 IR spectra of (a) parent adsorbent MgSi-b-*en*, (b) nickel ion loaded MgSi-b-*en*(+Ni), and (c) stripped nickel ion MgSi-b-*en*(-Ni)

Compared to MgSi-b-*en*, both the copper ion-imprinted and nickel ion-imprinted materials produced very similar TGA profiles (Figures 3.27 and 3.28, respectively). A slight deviation from the parent profile was exhibited by the Cu(II) and Ni(II) ion loaded adsorbents, MgSi-b-*en*(+Cu) and MgSi-b-*en*(+Ni), respectively. The weight loss resulting from the decomposition of organic groups occurred more rapidly, but the percentage lost remained the same. The accessibility of the organic groups seems to be altered in the imprinted process. The trend is also visible in the nickel ion-imprinted adsorbents, however the profile is not as greatly altered by the stripping method. Therefore it can be assumed that the presence of a metal ion exposes the organic groups more than in a non-imprinted material. The loaded materials, prior to leaching, have a morphology of closely packed sheets assembled side-by-side, rather than overlapped and

stacked onto one another. Thus, with a more exposed surface, the organic groups could burn off easier. It had also been established by N_2 adsorption isotherms that the loaded materials exhibited a lower degree of porosity, also suggesting more exposed surface functional groups. Upon leaching the Cu(II) and Ni(II) ions from the loaded adsorbents, the TGA profiles once again resemble the parent's pattern. It should also be noted that the weight loss of organic groups resulting from thermal decomposition is not altered during the imprinting procedure, so the same amount of chelating *en* groups are incorporated into each adsorbent.

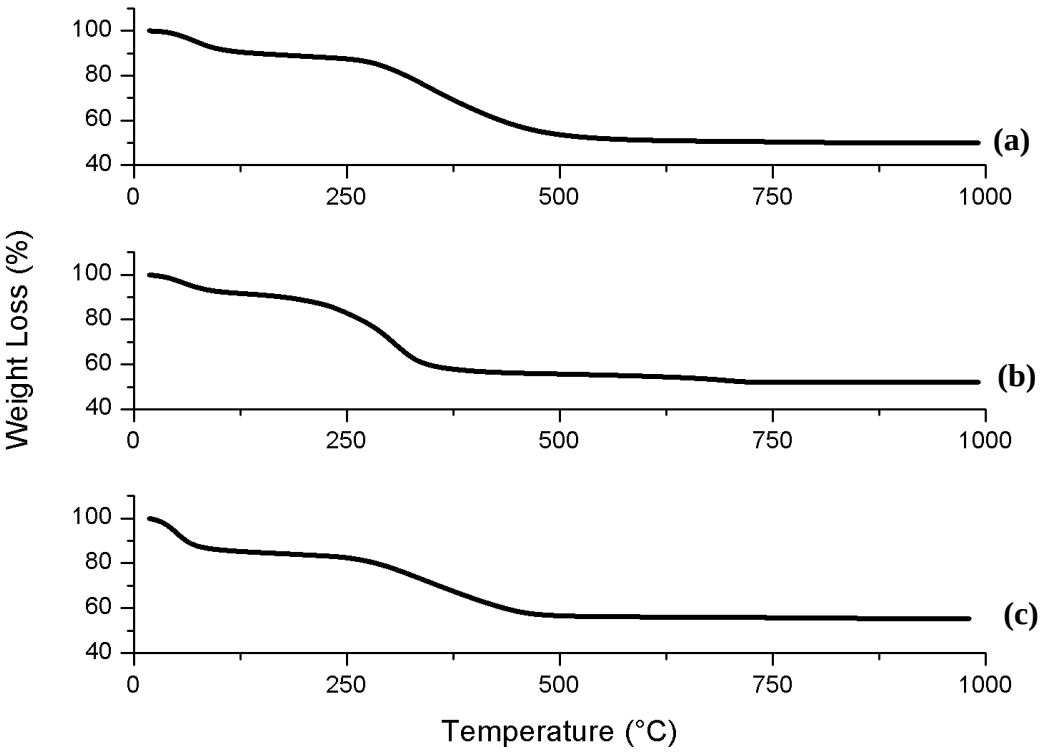

Figure 3.27 TGA profiles of (a) parent adsorbent MgSi-b-*en*, (b) copper ion loaded MgSi-b-*en*(+Cu), and (c) stripped copper ion MgSi-b-*en*(-Cu)

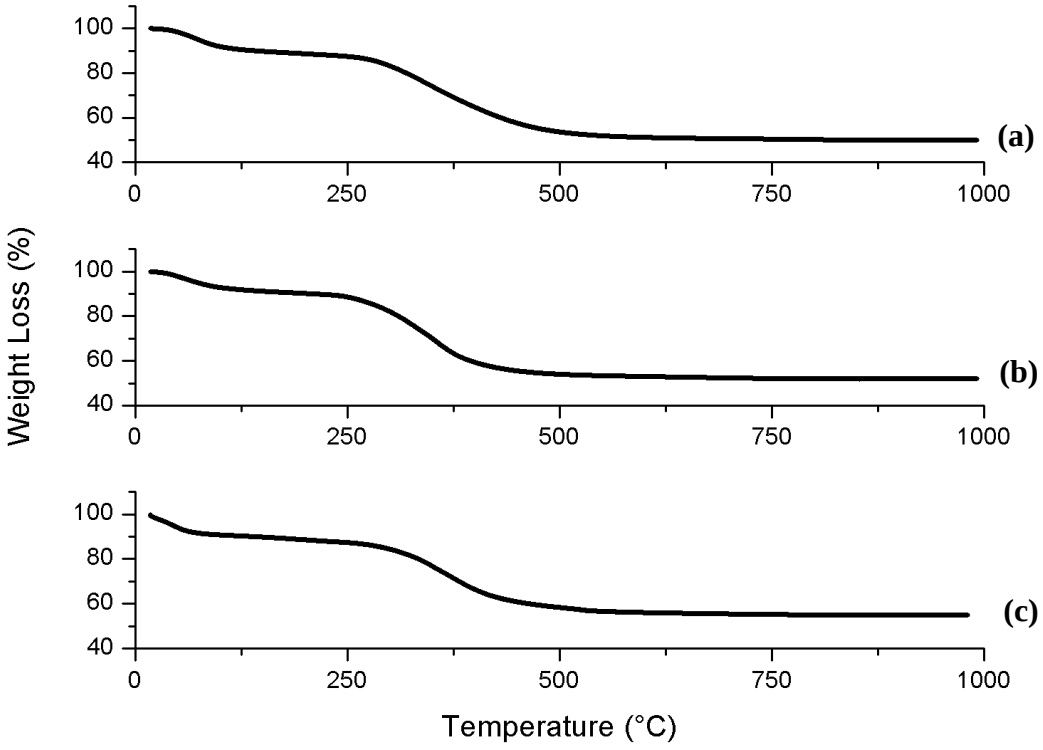

Figure 3.28 TGA profiles of (a) parent adsorbent MgSi-b-*en*, (b) nickel ion loaded MgSi-b-*en*(+Ni), and (c) stripped nickel ion MgSi-b-*en*(-Ni)

3.3.3 Altering Specificity of Heavy Metal Adsorption

The same multi-component adsorption tests done for MgSi-b-*en* (see *3.2.5 Multi-Component Adsorption*) were performed using the ion-imprinted organoclays. Adsorption capacity (Q_e), relative adsorption capacity (Q_e'), selectivity coefficient (k), and relative selectivity coefficient (k') were calculated in each binary metal system. The relative adsorption capacity and relative selectivity coefficient were calculated simply by dividing the Q_e and k of adsorption for the imprinted adsorbent by the respective Q_e and k for the parent adsorbent. Both of these values are indicative of the altered specificity induced by the ion-imprinted materials. Values above one indicate increased specificity towards a given metal ion relative to MgSi-b-*en*.

MgSi-b-*en*(-Cu) exhibited Q_e values of copper adsorption in Cu(II)/Ni(II) binary systems that were slightly lower than those for the parent adsorbent, clearly visible in the Q_e' values (Table 3.4). In spite of this, almost all of the copper-nickel solutions resulted in $k' > 1$, except for copper solutions at over-capacity coupled with low concentrations of nickel. In fact, the adsorbent surprisingly exhibited lower k' values with increasing copper concentrations. Though this seems to be counter-productive, increasing Ni(II) concentration in solution also lowered the adsorbent's specificity towards nickel. The specificity of MgSi-b-*en*(-Cu) towards copper ions from binary Cu(II)/Ni(II) systems was influenced more by the concentration of copper than nickel in solution. However, it was revealed that the adsorbent is more selective to either metal at lower concentrations. It could be suggested that active *en* sites on the imprinted adsorbent are less accessible to metal ions, as evidenced by characterization methods (notably the lack of porosity illustrated in the N_2 adsorption isotherm). Therefore the overall adsorption capacity of the adsorbent was lower than the parent organoclay.

(a)

	Q_e (mmol/g)	**Q_e'**	**k**	**k'**
Under-Capacity Cu(II)				
UCN	**1.05** ± 0.02	**0.68**	**6.7** ± 0.4	**2.28**
ACN	**1.12** ± 0.07	**0.85**	**11.1** ± 0.5	**5.43**
OCN	**1.135** ± 0.006	**0.98**	**17.3** ± 1.0	**10.62**
At-Capacity Cu(II)				
UCN	**2.10** ± 0.2	**1.10**	**6.36** ± 0.05	**1.05**
ACN	**1.97** ± 0.02	**1.04**	**9.3** ± 0.7	**2.07**
OCN	**1.838** ± 0.005	**0.95**	**11.9** ± 0.9	**3.83**
Over-Capacity Cu(II)				
UCN	**3.10** ± 0.04	**0.86**	**5.5** ± 0.5	**0.40**
ACN	**2.22** ± 0.02	**0.64**	**5.0** ± 0.7	**0.63**
OCN	**2.39** ± 0.08	**0.75**	**4.7** ± 0.8	**1.04**

(b)

	Q_e (mmol/g)	Q_e'	k	k'
Under-Capacity Ni(II)				
UCC	**0.627** ± 0.002	**1.20**	**0.149** ± 0.009	**0.44**
ACC	**0.52** ± 0.08	**1.52**	**0.1572** ± 0.0011	**0.95**
OCC	**0.403** ± 0.008	**1.32**	**0.165** ± 0.013	**2.27**
At-Capacity Ni(II)				
UCC	**0.88** ± 0.07	**1.26**	**0.090** ± 0.004	**0.18**
ACC	**0.66** ± 0.06	**1.41**	**0.107** ± 0.008	**0.48**
OCC	**0.56** ± 0.04	**1.13**	**0.18** ± 0.02	**1.44**
Over-Capacity Ni(II)				
UCC	**1.000** ± 0.013	**1.29**	**0.058** ± 0.003	**0.09**
ACC	**0.71** ± 0.11	**1.06**	**0.084** ± 0.006	**0.26**
OCC	**0.93** ± 0.07	**1.27**	**0.20** ± 0.03	**0.88**

Table 3.4 (a) Copper and (b) nickel adsorption capacities, selectivity constants, and relative selectivity constants of MgSi-b-*en*(-Cu) in binary Cu(II)/Ni(II) systems

The imprinted adsorbent MgSi-b-*en*(-Cu) showed increased specificity towards copper ions in Cu(II)/Pb(II) binary systems (Table 3.5). Unlike in the Cu(II)/Ni(II) solutions, nearly all of the systems exhibited $Q_e' > 1$. For all cases, $k' > 1$ as well, with specificity even increasing 18-fold in under-capacity solutions. Again, high concentrations correlated to decreasing selectivity coefficients, resembling the copper-nickel assays. The increased specificity of MgSi-b-*en*(-Cu) towards copper over lead was more significant, as both Q_e and k' for lead adsorption decreased relative to the parent adsorbent. The size difference between copper and lead ions most likely contributed to the increased specificity, and despite the overall inaccessibility of metal ions into the adsorbent, smaller copper ions can more easily penetrate the cavities produced by the imprinting procedure.

(a)

	Q_e (mmol/g)	Q_e'	K	k'
Under-Capacity Cu(II)				
UCP	**0.97** ± 0.13	**1.17**	**0.8** ± 0.3	**18.57**
ACP	**0.83** ± 0.06	**1.40**	**0.51** ± 0.11	**7.93**
OCP	**0.580** ± 0.014	**1.69**	**0.66** ± 0.11	**5.23**
At-Capacity Cu(II)				
UCP	**1.50** ± 0.07	**0.83**	**0.54** ± 0.10	**10.55**
ACP	**1.43** ± 0.15	**1.17**	**0.67** ± 0.10	**6.93**
OCP	**1.16** ± 0.18	**2.43**	**0.61** ± 0.09	**5.49**
Over-Capacity Cu(II)				
UCP	**2.24** ± 0.10	**1.04**	**0.82** ± 0.17	**7.44**
ACP	**2.23** ± 0.16	**1.14**	**0.58** ± 0.12	**4.05**
OCP	**2.0** ± 0.3	**1.52**	**0.63** ± 0.07	**2.71**

(b)

	Q_e (mmol/g)	Q_e'	k	k'
Under-Capacity Pb(II)				
UCC	**0.71** ± 0.10	**0.57**	**1.3** ± 0.5	**7.77×10^{-5}**
ACC	**0.79** ± 0.08	**0.67**	**1.9** ± 0.3	**1.00×10^{-4}**
OCC	**0.70** ± 0.11	**0.56**	**1.2** ± 0.3	**7.08×10^{-5}**
At-Capacity Pb(II)				
UCC	**1.55** ± 0.25	**0.67**	**2.0** ± 0.5	**1.29×10^{-4}**
ACC	**1.34** ± 0.10	**0.53**	**1.5** ± 0.3	**8.92×10^{-5}**
OCC	**1.4** ± 0.2	**0.59**	**1.7** ± 0.4	**1.40×10^{-4}**
Over-Capacity Pb(II)				
UCC	**1.8** ± 0.4	**0.57**	**1.5** ± 0.3	**8.15×10^{-5}**
ACC	**1.9** ± 0.2	**0.64**	**1.6** ± 0.3	**8.19×10^{-5}**
OCC	**1.70** ± 0.13	**0.65**	**1.6** ± 0.2	**1.38×10^{-4}**

Table 3.5 (a) Copper and (b) lead adsorption capacities, selectivity constants, and relative selectivity constants of MgSi-b-*en*(-Cu) in binary Cu(II)/Pb(II) systems

MgSi-b-*en*(-Ni) in binary Cu(II)/Ni(II) systems revealed increased adsorption capacity and specificity towards nickel ions (Table 3.6). Almost all of the Q_e values for nickel adsorption were higher than the parent adsorbent's Q_e ($Q_e' > 1$). Unfortunately, increased specificity towards nickel in the binary solutions was only observed in

solutions containing high concentrations of copper. Furthermore, the copper solutions at under-capacity all had resulting $k' > 1$. However, an exclusion of Cu(II) ions by the adsorbent was observed, as the adsorption capacities for copper were lower in all concentrations. The same trend of lower k' relative to increasing overall metal ion concentrations in solution was also prevalent throughout the binary test.

(a)

	Q_e (mmol/g)	Q_e'	k	k'
Under-Capacity Cu(II)				
UCN	**1.00** ± 0.06	**0.64**	**5.0** ± 0.9	**1.69**
ACN	**0.88** ± 0.04	**0.67**	**4.9** ± 0.5	**2.40**
OCN	**0.84** ± 0.04	**0.73**	**6.2** ± 0.9	**3.83**
At-Capacity Cu(II)				
UCN	**1.57** ± 0.05	**0.82**	**4.3** ± 0.5	**0.71**
ACN	**1.55** ± 0.06	**0.82**	**4.5** ± 0.5	**0.99**
OCN	**1.46** ± 0.07	**0.76**	**4.4** ± 0.6	**1.42**
Over-Capacity Cu(II)				
UCN	**2.52** ± 0.14	**0.70**	**5.43** ± 1.0	**0.39**
ACN	**1.88** ± 0.18	**0.54**	**4.5** ± 1.2	**0.56**
OCN	**1.87** ± 0.15	**0.59**	**2.4** ± 0.3	**0.53**

(b)

	Q_e (mmol/g)	Q_e'	k	k'
Under-Capacity Ni(II)				
UCC	**0.57** ± 0.02	**1.10**	**0.20** ± 0.04	**0.59**
ACC	**0.36** ± 0.04	**1.04**	**0.23** ± 0.02	**1.40**
OCC	**0.309** ± 0.006	**1.01**	**0.18** ± 0.03	**2.54**
At-Capacity Ni(II)				
UCC	**0.75** ± 0.11	**1.07**	**0.20** ± 0.02	**0.42**
ACC	**0.61** ± 0.05	**1.31**	**0.22** ± 0.02	**1.01**
OCC	**0.46** ± 0.05	**0.93**	**0.22** ± 0.07	**1.79**
Over-Capacity Ni(II)				
UCC	**0.89** ± 0.04	**1.15**	**0.16** ± 0.02	**0.26**
ACC	**0.94** ± 0.12	**1.41**	**0.23** ± 0.04	**0.71**
OCC	**1.05** ± 0.03	**1.42**	**0.42** ± 0.05	**1.90**

Table 3.6 (a) Copper and (b) nickel adsorption capacities, selectivity constants, and relative selectivity constants of MgSi-b-*en*(-Ni) in binary Cu(II)/Ni(II) systems

Finally, the nickel ion-imprinted adsorbent, MgSi-b-*en*(-Ni), on the Ni(II)/Pb(II) binary systems displayed the largest increase in specificity over the parent adsorbent (Table 3.7) for all degrees of capacity, every $Q_e' > 1$ and $k' > 1$. Like copper-lead systems, the size difference between nickel and lead ions produced favourable results. In addition to higher capacities and specificity, the adsorbent also excluded the adsorption of lead ions, as shown by the low relative capacities and selectivity coefficients.

(a)

	Q_e (mmol/g)	Q_e'	k	k'
Under-Capacity Ni(II)				
UCP	**0.5** ± 0.3	**1.30**	**0.23** ± 0.17	**204.90**
ACP	**0.3** ± 0.3	**1.75**	**0.09** ± 0.16	**10.10**
OCP	**0.24** ± 0.18	**2.53**	**0.06** ± 0.15	**1.99**
At-Capacity Ni(II)				
UCP	**0.9** ± 0.6	**1.53**	**0.15** ± 0.17	**99.01**
ACP	**0.7** ± 0.3	**2.10**	**0.17** ± 0.12	**21.18**
OCP	**0.6** ± 0.3	**2.59**	**0.18** ± 0.16	**4.26**
Over-Capacity Ni(II)				
UCP	**1.0** ± 0.3	**1.42**	**0.17** ± 0.04	**92.52**
ACP	**0.73** ± 0.11	**1.79**	**0.10** ± 0.02	**12.42**
OCP	**0.43** ± 0.07	**1.63**	**0.073** ± 0.0013	**1.61**

(b)

	Q_e (mmol/g)	Q_e'	k	k'
Under-Capacity Pb(II)				
UCN	**1.01** ± 0.17	**0.81**	**4** ± 2	**4.88×10^{-3}**
ACN	**1.0** ± 0.3	**0.76**	**7** ± 3	**1.01×10^{-2}**
OCN	**0.82** ± 0.14	**0.55**	**6** ± 1	**1.08×10^{-2}**
At-Capacity Pb(II)				
UCN	**1.5** ± 0.7	**0.64**	**18** ± 8	**6.10×10^{-2}**
ACN	**1.6** ± 0.4	**0.63**	**6** ± 3	**4.72×10^{-2}**
OCN	**1.7** ± 0.4	**0.59**	**10** ± 2	**8.05×10^{-2}**
Over-Capacity Pb(II)				
UCN	**2.0** ± 0.4	**0.65**	**15** ± 2	**0.50**
ACN	**1.9** ± 0.4	**0.66**	**6** ± 3	**0.23**
OCN	**2.0** ± 0.3	**0.73**	**13.8** ± 0.2	**0.62**

Table 3.7 (a) Nickel and (b) lead adsorption capacities, selectivity constants, and relative selectivity constants of MgSi-b-*en*(-Ni) in binary Ni(II)/Pb(II) systems

4. Summary and Conclusions

An ethylenediamine-functionalized clay was synthesized via the sol-gel method. The synthetic silicate material was designed to resemble the chemical formula of natural talc, $Mg_3Si_4O_{10}(OH)_2$. Contrary to the traditional mono-substituted organosilanes that have previously been employed in organoclay synthesis, a bridged or "bis" organosilane was used. The bis-silane, which contained the chelating ligand *en*, was denoted as MgSi-b-*en*. MgSi-b-*en* did not exhibited lamellar stacking of the formed magnesium phyllosilicate layers. However, due to the incorporation of the chelating agent into the clay structure, the material was proven to be an effective adsorbent for heavy metal ions in aqueous media. The presence of the organic moieties in the material was confirmed by multiple characterization techniques.

MgSi-b-*en* selectively adsorbed copper, nickel, and lead ions with rapid uptake times and very high adsorption capacities. For copper and lead, the adsorption capacities exhibited by the material were considerably higher than expected. This led to the conclusion that the adsorption of metal ions operates by means of chemisorption followed by physical interactions. The specificity of the adsorbent towards a single ion was tested in binary metal systems, revealing that the MgSi-b-*en* preferentially adsorbed the three metals in the following order:

$$Pb^{2+} > Cu^{2+} > Ni^{2+}$$

The specificity of the ethylenediamine-functionalized adsorbent was altered by an ion-imprinting technique. Inclusion of a given metal in the synthesis resulted in the complexation of the organosilane precursor with the ion prior to condensation. The organoclay was then formed pre-loaded with metal ions, and upon leaching, a cavity was

left in the structure. Because a bis-silane was used, the organic groups were likely to be anchored in place to maintain the shape of this cavity. Binary adsorption tests were again performed to confirm the altered specificity brought out by the imprinting method. Comparing the selectivity coefficients of the imprinted adsorbents to the parent adsorbent, MgSi-b-*en*, gave impressive results. The specificity of the imprinted adsorbents were in fact altered. In most cases (depending on degree of capacity of the metal ions in solution) both the copper and nickel-imprinted adsorbents exhibited higher selectivity coefficients towards Cu(II) and Ni(II) ions, respectively. The altered specificity was most apparent in binary systems containing the much larger Pb(II) ion. The smaller cavities produced by the ion-imprinting technique (with copper and nickel ions) not only resulted in higher selectivity coefficients, but also higher adsorption capacities for their respective metal ions.

Although the organoclays synthesized did not exhibit the typical lamellar stacking of natural talc, they were excellent adsorbents. Because of formation of an inorganic backbone, a much higher loading of *en* ligands was able to be incorporated into the clay structure. The ion-imprinting technique was possible on these materials as well, and even though the metal ions could not be totally desorbed from the loaded adsorbent, the stripped materials proved to be effective adsorbents for specific metal ions.

5. References

1. R. W. Tschernich, *Zeolites of the World* (1992) Geoscience Press Inc., Phoenix, AZ, 565p.

2. M. E. Davis, R. F. Lobo, *Chem. Mater.*, 4 (1992) 756-758.

3. A. Corma, *Chem. Rev.*, 97 (1997) 2373-2419.

4. L. Curkovic, S. Cerjan-Stefanovic, T. Filipan, *Wat. Res.*, 31 (199&0 1379-1382.

5. D. Kallo, *Reviews in Minerology and Geochemistry*, 45 (2001) 519-550.

6. T. J. Pinnavaia, *Science*, 220 (1983) 365–371.

7. K. Tanabe, J. R. Anderson, M. Boudart, *Catalysis - Science and Technology*, (1981) 231.

8. S. E. Bailey, T. J. Olin, R. M. Bricka, D. D. Adrian, *Water Research*, 33 (1999) 2469-2479.

9. R. K. Iler, *The Chemistry of Silica* (1979) Plenum Press, John Wiley & Sons, New York, 790p.

10. J. S. Beck, J. C. Vartuli, W. J. Roth, M. W. Leonowicz, C. T. Kresge, K. D. Schmitt, C. T-W. Chu, D. H. Olson, E. W. Sheppard, S. B. McCullen, J. B. Higgins, J. L. Schlenker, *J. Am. Chem. Soc.*, 114 (1992) 10834-10843.

11. C. T. Kresge, M. E. Leonowicz, W. J. Roth, J. C. Vartuli, J. S. Beck, *Nature*, 359 (1992) 710-712.

12. M. Dubois, T. Gulik-Krzywicki, B. Cabane, *Langmuir*, 9 (1993) 673-680.

13. J. C. Vartuli, K. D. Schmitt, C. T. Kresge, W. J. Roth, M. E. Leonowicz, S. B. McCullen, S. D. Hellring, J. S. Beck, J. L Schlenker, D. H. Olson, E. W. Sheppard, *Chem. Mater.*, 6 (1994) 2317-2326.

14. X. S. Zhao, G. Q. Lu, G. J. Millar, *Ind. Eng. Chem. Res.*, 35 (1996) 2075-2090.

15. C. Gao, H. Qiu, W. Zeng, Y. Sakamoto, O. Terasaki, K. Sakamoto, Q. Chen, S. Che, *Chem. Mater.*, 18 (2006) 3904-3914.

16. D. Zhao, J. Feng, Q. Huo, N. Melosh, G. H. Fredrickson, B. F. Chmelka, G. D. Stucky, *Science*, 279 (1998) 548-552.

17. D. Zhao, Q. Huo, J. Feng, B. F. Chmelka, G. D. Stucky, *J. Am. Chem. Soc.*, 120 (1998) 6024-6036.

18. S. A. Bagshaw, E. Prouzet, T. Pinnavaia, *Science*, 269 (1995) 1242-1244.

19. E. Prouzet, T. Pinnavaia, *Angew. Chem. Int. Ed. Engl.*, 36 (1997) 516-518.

20. P. T. Tanev, T. Pinnavaia, *Chem. Mater.*, 8 (1996) 2068-2079.

21. T. R. Pauly, T. Pinnavaia, *Chem. Mater.*, 13 (2001) 987-993.

22. A. Stein, B. J. Melde, R. C. Schroden, *Adv. Mater.*, 19 (2000) 1403-1419.

23. L. Mercier, T. J. Pinnavaia, *Environ. Sci. Technol.*, 32 (1998) 2749-2754.

24. A. Walcarius, L. Mercier. *J. Mater. Chem.*, 20 (2010) 4478-4511.

25. J. Brown, R. Richer, L. Mercier, *Microporous and Mesoporous Materials*, 37 (2000) 41-48.

26. B. J. Melde, B. T. Holland, C. F. Blanford, A. Stein, *Chem. Mater.*, 11 (1999) 3302-3308.

27. T. Asefa, M. J. MacLachlan, N. Coombs, G. A. Ozin, *Nature*, 402 (1999) 867-871.

28. C. E. Weaver, *Clays, Muds, and Shales* (1989) Elsevier Science Publishing Company Inc., New York, 819p.

29. L. Mercier, C. Detellier, *Environ. Sci. Technol.*, 29 (1995) 1318-1323.

30. L. Mercier, T. Pinnavaia, *Microporous and Mesoporous Materials*, 20 (1998) 101-106.

31. A. J. Schwanke, S. B. C. Pergher, *Ceramica*, 59 (2013) 576-587.

32. A. J. Tchinda, E. Ngameni, I. T. Kenfack, A. Walcarius, *Chem. Mater.*, 21 (2009) 4111-4121.

33. T. Mizutani, Y. Fukushima, A. Okada, O. Kamigaito, *Bull. Chem. Soc. Jpn.*, 63 (1990) 2094.

34. Y. Fukushima, M. Tani, *Chem. Commun.* (1995) 241-242.

35. J. A. A. Sales, G. C. Petrucelli, F. J. V. E. Oliveira, C. Airoldi, *Journal of Colloid and Interface Science*, 297 (2006) 95-103.

36. M. G. da Fonseca, C. R. Silva, C. Airoldi, *Langmuir*, 15 (1999) 5048-5055.

37. L. Ukrainczyk, R. A. Bellman, A. B. Anderson, *J. Phys. Chem. B*, 101 (1997) 531-539.

38. M. Jaber, J. Miehe-Brendle, L. Delmotte, R. Le Dred, *Solid State Sciences*, 7 (2005) 610-615.

39. M. Jaber, J. Miehe-Brendle, L. Michelin, L. Delmotte, *Chem. Mater.*, 17 (2005) 5275-5281.

40. A. J. Patil, S. Mann, *J. Mater. Chem.*, 18 (2008) 4605-4615.

41. C. R. Silva, M. G. Fonseca, J. S. Barone, C. Airoldi, *Chem. Mater.*, 14 (2002 175-179.

42. P. T. Tanev, M. Chibwe, T. J. Pinnavaia, *Nature*, 368 (1994) 321-323.

43. C. Breen, R. Watson, J. Madejova, P. Komadel, Z. Klapyta, *Langmuir*, 13 (1997) 6473-6479.

44. I. I. Slowing, J. L. Vivero-Escoto, C-W. Wu, V. S-Y. Lin, *Advanced Drug Delivery Reviews*, 60 (2008) 1278-1288.

45. H. A. Patel, R. S. Somani, H. C. Bajaj, R. V. Jasra, *Bull. Mater. Sci.*, 29 (2006) 133-145.

46. N. D. Tumin, A. L. Chuah, Z. Zawani, S. A. Rashid, *Journal of Engineering Science and Technology*, 3 (2008) 180-189.\

47. J. C. Y. Ng, W. H. Cheung, G. McKay, *Journal of Colloid and Interface Science*, 255 (2002) 64-74.

48. M. Poonkothai, B. S. Vijayavathi, *Internation Journal of Environmental Sciences*, 1 (2012) 285-288.

49. H. Hasar, *Journal of Hazardous Materials*, B97 (2003) 49-57.

50. Z-H. Huang, X. Zheng, W. Lv, M. Wang, Q-H. Yang, F. Kang, *Langmuir*, 27 (2011) 7558-7562.

51. Y-H. Li, S. Wang, J. Wei, X. Zhang, C. Xu, Z. Luan, D. Wu, B. Wei, *Chemical Physics Letters*, 357 (2002) 263-266.

52. K. Z. Hossain, L. Mercier, *Adv. Mater.*, 14 (2002) 1053-1056.

53. Z. Wang, G. Wu, M. Wang, C. He, *J. Mater. Sci.*, 44 (2009) 2694-2699.

54. S. Dai, M. C. Burleigh, Y. Shin, C. C. Morrow, C. E. Barnes, Z. Xue, *Angew. Chem. Int. Ed.*, 38 (1999) 1235-1239.

55. S. Brunauer, P. H. Emmett, E. Teller, *J. Am. Chem. Soc.*, 60 (1938) 309-319.

56. P. Atkins, J. de Paula, *Physical Chemistry* (2010) W. H. Freeman and Company, New York, 1010p.

57. J. Goldstein, *Scanning Electron Microscopy and X-ray Microanalysis: Third Edition* (2003) Springer US, 689p.

58. Y. S. Ho, G. McKay, *Process Biochemistry*, 34 (1999) 451-465.

59. Y. S. Ho, G. McKay, *Trans IChemE*, 76 (1998) 332-340.

60. K. Y. Foo, B. H. Hameed, *Chemical Engineering Journal*, 156 (2010) 2-10.

61. S. J. Allen, G. McKay, J. F. Porter, *Journal of Colloid and Interface Science*, 280 (2004) 322-333.

62. M. R. Bhambhani, P. A. Cutting, K. S. W. Sing, D. H. Turk, *Journal of Colloid and Interface Science*, 38 (1972) 109-117.

63. G. Socrates, *Infrared and Raman Characteristic Group Frequencies: Tables and Charts* (2004) John Wiley & Sons, New York, 347p.

64. D-H. Chen, S-H. Wu, *Chem. Mater.*, 12 (2000) 1354-1360.

65. G-X. Zhu, X-W. Wei, S. Jiang, *J. Mater. Chem.*, 17 (2007) 2301-2306.

66. C. C. Addison, B. M. Gatehouse, *J. Chem. Soc.*, 0 (1960) 613-616.